JGR Space Physics

RESEARCH ARTICLE
10.1029/2022JA031138

Key Points:

- Modeled secondary gravity waves (GWs) radiate globally from Tonga with $c_H \sim 100$–600 m/s, $\lambda_H \sim 400$–7,500 km, and $\tau_r \sim 20$ min to 7 hr
- ICON observed northeastward GWs from Tonga with $c_H \sim 100$–600 m/s and $\lambda_H \sim 800$–7,500 km, in good agreement with the model
- Temporally and spatially variable large-scale wind changes of ~80–120 m/s are created by the dissipation of the secondary GWs

Supporting Information:

Supporting Information may be found in the online version of this article.

Correspondence to:
S. L. Vadas,
vasha@nwra.com

Citation:
Vadas, S. L., Becker, E., Figueiredo, C., Bossert, K., Harding, B. J., & Gasque, L. C. (2023). Primary and secondary gravity waves and large-scale wind changes generated by the Tonga volcanic eruption on 15 January 2022: Modeling and comparison with ICON-MIGHTI winds. *Journal of Geophysical Research: Space Physics*, *128*, e2022JA031138. https://doi.org/10.1029/2022JA031138

Received 6 NOV 2022
Accepted 21 JAN 2023

Author Contributions:
Conceptualization: Sharon L. Vadas
Data curation: Sharon L. Vadas
Formal analysis: Sharon L. Vadas, Cosme Figueiredo, Katrina Bossert
Investigation: Sharon L. Vadas, Cosme Figueiredo
Methodology: Sharon L. Vadas, Erich Becker, Katrina Bossert
Project Administration: Sharon L. Vadas
Resources: Sharon L. Vadas, Erich Becker, Cosme Figueiredo
Software: Sharon L. Vadas, Erich Becker
Supervision: Sharon L. Vadas
Validation: Sharon L. Vadas

Primary and Secondary Gravity Waves and Large-Scale Wind Changes Generated by the Tonga Volcanic Eruption on 15 January 2022: Modeling and Comparison With ICON-MIGHTI Winds

Sharon L. Vadas[1], **Erich Becker**[1], **Cosme Figueiredo**[2], **Katrina Bossert**[3], **Brian J. Harding**[4], **and L. Claire Gasque**[4]

[1]Northwest Research Associates, Boulder, CO, USA, [2]National Institute for Space Research, INPE, São José dos Campos, Brazil, [3]School of Earth and Space Exploration, School of Mathematical and Statistical Sciences, Arizona State University, Tempe, AZ, USA, [4]University of California, Berkeley, Berkeley, CA, USA

Abstract We simulate the primary and secondary atmospheric gravity waves (GWs) excited by the upward movement of air generated by the Hunga Tonga-Hunga Ha'apai (hereafter "Tonga") volcanic eruption on 15 January 2022. The Model for gravity wavE SOurce, Ray trAcing and reConstruction (MESORAC) is used to calculate the primary GWs and the local body forces/heatings generated where they dissipate. We add these forces/heatings to the HIgh Altitude Mechanistic general Circulation Model (HIAMCM) to determine the secondary GWs and large-scale wind changes that result. We find that a wide range of medium to large-scale secondary GWs with concentric ring structure are created having horizontal wind amplitudes of u', $v' \sim 100$–200 m/s, ground-based periods of $\tau_r \sim 20$ min to 7 hr, horizontal phase speeds of $c_H \sim 100$–600 m/s, and horizontal wavelengths of $\lambda_H \sim 400$–7,500 km. The fastest secondary GWs with $c_H \sim 500$–600 m/s are large-scale GWs with $\lambda_H \sim 3{,}000$–7,500 km and $\tau_r \sim 1.5$–7 hr. They reach the antipode over Africa ~9 hr after creation. Large-scale temporally and spatially varying wind changes of ~80–120 m/s are created where the secondary GWs dissipate. We analyze the Tonga waves measured by the Michelson Interferometer for Global High-resolution Thermospheric Imaging (MIGHTI) on the National Aeronautics and Space Administration Ionospheric Connection Explorer (ICON), and find that the observed GWs were medium to large-scale with $c_H \sim 100$–600 m/s and $\lambda_H \sim 800$–7,500 km, in good agreement with the simulated secondary GWs. We also find good agreement between ICON-MIGHTI and HIAMCM for the timing, amplitudes, locations, and wavelengths of the Tonga waves, provided we increase the GW amplitudes by ~2 and sample them ~30 min later than ICON.

Plain Language Summary Atmospheric gravity waves (GWs) are buoyancy driven perturbations in the Earth's atmosphere that can be created by various processes. GW breaking is similar to the breaking of ocean waves when they overturn. A breaking GW imparts momentum to the ambient atmosphere, which can create secondary GWs. We simulated the Tonga eruption on 15 January 2022 using Geostationary Operational Environmental Satellite satellite images, ray tracing, and a GW-resolving global circulation model. We find that the secondary GWs created by the breaking of the primary GWs from the eruption propagated globally and changed the large-scale wind patterns in the thermosphere. Furthermore, the phase speeds and wavelengths of these waves simulated by the model agree well with corresponding results from ICON satellite measurements. Thus, this study highlights the importance of a process called "multi-step vertical coupling", according to which secondary GWs are important drivers in the Earth's thermosphere.

1. Introduction

On 15 January 2022, a submarine volcano erupted many times at Hunga Tonga-Hunga Ha'apai at 20.54°S and 184.62°E from ~4–5 UT (Astafyeva et al., 2022), thereby creating acoustic waves (including Lamb waves) and atmospheric gravity waves (GWs) that propagated into the stratosphere and thermosphere and over the whole globe (Lin et al., 2022; Themens et al., 2022; Wright et al., 2022; Zhang et al., 2022). The Lamb waves were observed propagating globally near the Earth's surface for ~6 days after the eruption (Amores et al., 2022). This was a unique and important event because there had been no prior observational evidence of GW propagation over distances >3,000 km from volcanic eruptions (Wright et al., 2022; Zhang et al., 2022).

Visualization: Sharon L. Vadas, L. Claire Gasque
Writing – original draft: Sharon L. Vadas
Writing – review & editing: Sharon L. Vadas, Erich Becker, Cosme Figueiredo, Katrina Bossert, Brian J. Harding, L. Claire Gasque

Many studies analyzed the traveling ionospheric disturbances (TIDs) induced from the Tonga waves via analyzing GPS/TEC data. Wright et al. (2022) observed three TIDs from Tonga with $c_H \sim 667$, 414, and 343 m/s over New Zealand. Although they saw the second and third TIDs over North America, they did not observe the first TID there. They also observed a Lamb wave in the troposphere and stratosphere, which is a special type of acoustic wave that propagates at the sound speed in the horizontal direction only. They found that the Lamb wave propagated three times around the Earth, with $c_H \sim 300$–320 m/s and $\lambda_H \sim 150$ km. Themens et al. (2022) observed several LSTIDs within 3,000 km of the epicenter with $c_H \sim 950$ and 555 m/s and $\lambda_H > 1{,}600$ km. They also observed MSTIDs with $c_H \sim 200$–400 m/s for ∼6 hr after the eruptions. They found that the LSTIDs were distributed non-symmetrically, being barely discernible in Australia and completely absent in Africa, whereas the MSTIDs were symmetrically distributed. They did not observe MSTIDs with $c_H > 400$ m/s at distances >4,000 km from the epicenter, however. Zhang et al. (2022) analyzed MSTIDs with $\tau_r \sim 10$–30 min from Tonga, and found they had horizontal phase speeds up to $c_H \sim 700$ m/s within 4,000 km of the epicenter, but otherwise had $c_H \sim 350$ m/s at distances further away. They found that these latter waves propagated around the Earth three times over 4 days, re-passing over Tonga every 1.5 days. Lin et al. (2022) analyzed the TIDs with $\tau_r \sim 12$–20 and 30–50 min, and found that these waves had $c_H \sim 320$–390 m/s. They also observed conjugate MSTIDs over Japan at 8:00–11:00 UT. It is important to emphasize that these latter three studies did not analyze TIDs with $\tau_r > 1$ hr. This analysis limitation significantly restricted the scope of their studies because the fastest GWs to reach the F region at large distances from Tonga have $\tau_r > 1$ hr, as we show in this paper.

Harding et al. (2022) analyzed the neutral zonal winds measured by ICON-MIGHTI during orbit #s 12371 and 12372 at 13:45–17:00 UT on 15 January 2022. They identified coherent waves from Tonga spanning $z = 110$–300 km at 50°–130°W having large amplitudes of $u' \sim 100$–150 m/s. They estimated large along-track wavelengths of $\lambda_{\text{track}} \sim 3{,}000$–5,000 km at $z > 120$ km. Gasque et al. (2022) inferred neutral horizontal wind velocities of >200 m/s in the E region ($z \sim 120$ km) at approximately ∼400 km from Tonga shortly after the Tonga eruption by analyzing ionospheric dynamo-induced plasma drifts measured by ICON's Ion Velocity Meter.

In this study, we model the primary and secondary GWs created by the eruption of the Tonga volcano on 15 January 2022 using the MESORAC and HIAMCM models. Section 2 introduces our methodology and discusses the primary GWs, and Section 3 analyzes the secondary GWs created by Tonga. The temporally variable large-scale changes of the thermospheric horizontal wind are discussed in Section 4. Section 5 analyzes the properties of the GWs observed by ICON and compares the ICON observations with the model results. A discussion and our conclusions are contained in Sections 6 and 7, respectively.

2. Methodology: GW Models and Data

2.1. Model: Primary GWs From Tonga

The Model for gravity wavE SOurce, Ray trAcing and reConstruction (MESORAC) calculates the primary GWs created from localized (in space and time) vertical updrafts of air using the Fourier-Laplace analytical fully compressible solutions (Vadas, 2013). These updrafts, which are mechanical displacements of stratospheric/mesospheric air, are identified from NOAA's Geostationary Operational Environmental Satellite (GOES) data. The atmosphere responds by radiating concentric rings of GWs (Vadas et al., 2012, 2009). MESORAC ray traces these GWs forward in time, including their phases, and reconstructs the primary GW field using the GW phases and the GW dissipative dispersion and polarization relations (Vadas & Fritts, 2005, 2009). The background atmosphere is taken from the HIgh Altitude Mechanistic general Circulation Model (HIAMCM) simulation for 15 January 2022 without the Tonga eruption (base case) using scales with $\lambda_H > 2{,}000$ km. Wave dissipation is due to molecular diffusion and turbulent diffusion from saturation. The latter is calculated from the convective instability criterion for the superposition of the background atmosphere and the reconstructed GW field:

$$D = \max\left\{0, -D_0\left[\frac{C_p}{g}\left(\frac{d\overline{T}}{dz} + \frac{dT'}{dz}\right) - a\right]\right\}, \tag{1}$$

where $T = \overline{T} + T'$ is the temperature, overlines denote unperturbed values, primes denote perturbations, C_p is the specific heat at constant pressure, g is the gravitational acceleration ($= 9.81$ m/s^2 at sea level), and $D_0 = 2{,}000$ m^2/s is a tunable turbulent diffusion parameter. $a = 0.7$ is a non-dimensional tunable threshold for saturation that has been found to be 0.7–1 in wave breaking simulations (for example, Achatz, 2007). Note that although our model

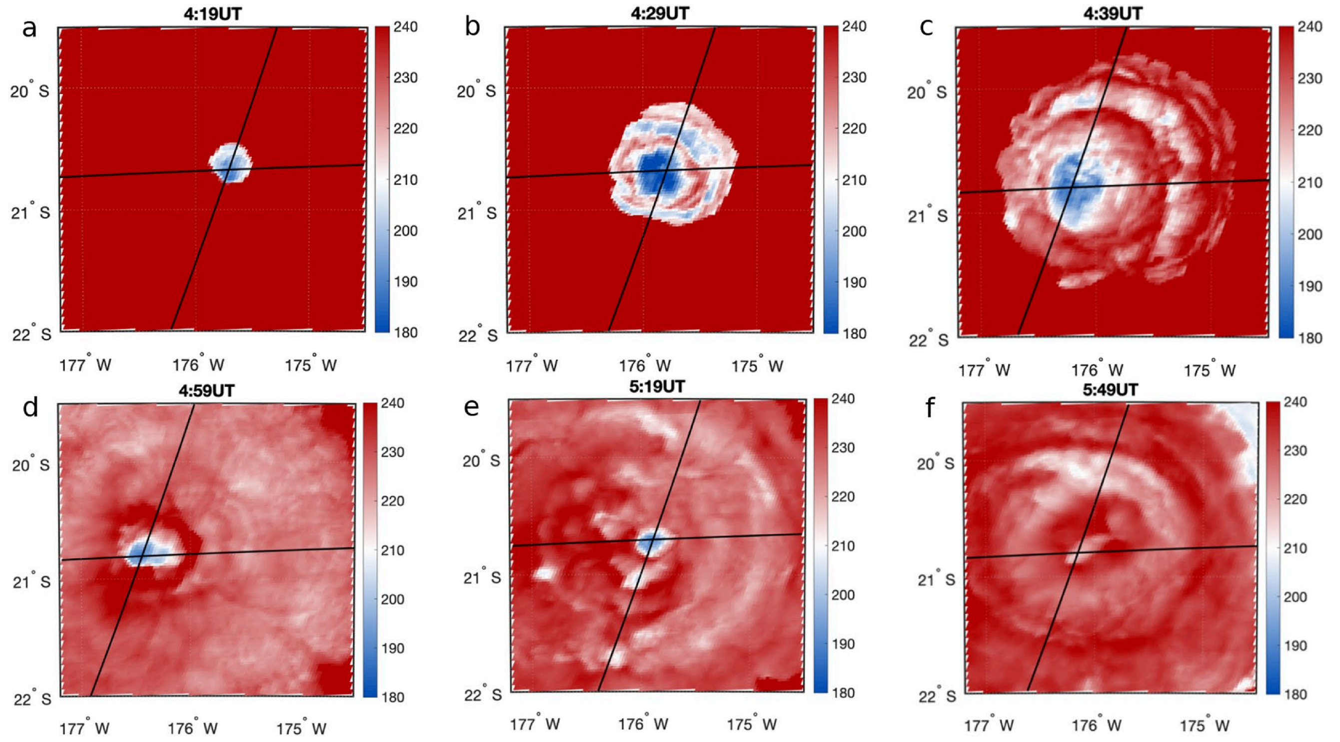

Figure 1. (a–f) Images of the cloud top brightness temperature T (in K) as functions of longitude and latitude derived from GOES-17 satellite data on 15 January 2022 at 4:19, 4:29, 4:39, 4:59, 5:19, and 5:49 UT, respectively. The black lines show the constant longitude/latitude lines that intersect the centers of the updrafts (plumes) from the Tonga eruption.

results depend significantly on D_0, they are fairly insensitive to the value of a. D_0 is tuned to 2,000 m^2/s because it results in GW amplitudes that are closest to the ICON-MIGHTI amplitudes without destabilizing the HIAMCM (see Section 5); larger values of D_0 result in smaller GW amplitudes, which is inconsistent with the ICON data. Once D is obtained (as functions of latitude, longitude, z and t), D is applied as an isotropic (vertical and horizontal) turbulent viscosity by adding it to the kinematic viscosity, ν (i.e., by replacing ν with $\nu + D$), and as an isotropic turbulent diffusivity by adding it to the thermal diffusivity (i.e., by replacing ν/Pr with $(\nu + D)$/Pr). Then the ray tracing is repeated. The body forces and heatings created by the dissipation of primary GWs are calculated as functions of space and time as in Vadas (2013). These ambient-flow effects are then added to the momentum and thermodynamic equations of the HIAMCM to simulate the secondary GWs from the Tonga eruption.

The first of many eruptions occurred at ~4:15 UT (Astafyeva et al., 2022). Here, we only consider the GWs excited by the mechanical displacement of air from 4:15–5:50 UT, not by the deep convection that ensued many hours later from the injection of water into the troposphere and stratosphere by the eruptions (Wright et al., 2022); this is due to the difficulty of determining the updraft parameters of the deep convective plumes from the GOES-17 images. Figure 1 shows the cloud top brightness temperatures, T, extracted from GOES-17 satellite data (available every 10 min) for six times between 4:19 and 5:49 UT where mechanical updrafts likely occurred. A very cold region appears at the center of each identified updraft (dark blue). Because each updraft (plume) is expected to create a cold spot on GOES-17 cloud-top images for a few to 5 min, we consider these updrafts as six individual plumes for the purposes of input into MESORAC. The plume diameter, $\mathcal{D}_H = 4.5\sigma_H$, is determined from the full width of each dark blue region in Figure 1 via visual inspection. Here, σ_H is the half-width of the Gaussian distribution of the cold region in the horizontal plane. These diameters range from $\mathcal{D}_H = 25$ to 40 km.

The first few updrafts from the Tonga eruption reached $z \sim 58$ km in the lower mesosphere (https://earthobservatory.nasa.gov/images/149474/tonga-volcano-plume-reached-the-mesosphere), or 50–55 km according to Carr et al. (2022). Note that concentric rings of primary GWs generated from previous updrafts appear as light blue and red concentric rings (4:29 UT and later) in Figure 1. For modeling the primary GWs created by these updrafts in MESORAC, we estimate the following plume parameters. Because the plume top is $z \sim 58$ km, we choose to launch (ray-trace) the GWs from $z = 30$ km, which is the approximate mid-point of the plumes in

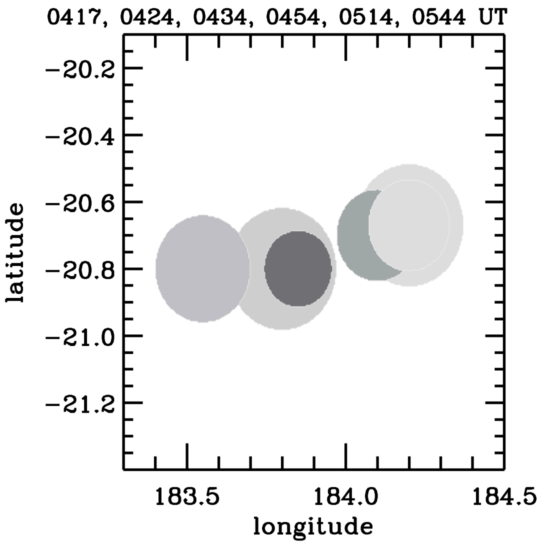

Figure 2. Locations and diameters of the updrafts from the Tonga eruption on 15 January 2022 identified from Figure 1. The vertical updrafts are modeled as single plumes with diameters ranging from $\mathcal{D}_H = 25 - 40$ km. The times of the plumes, which are 04:17, 04:24, 04:34, 04:54, 05:14, and 05:44 UT, are shown with light to dark shading, respectively.

altitude. This fits the MESORAC assumption that each plume is a Gaussian distribution in the vertical and horizontal directions. We also choose a primary GW launch time to be approximately halfway between the eruption time and the GOES image time for the first updraft, and to be approximately halfway between the current and previous GOES image times for the following updrafts. We choose this "halfway" time because (a) the updraft may have been at this altitude (likely $z > 50$ km according to the above NASA study) for 1–2 min when the GOES image was taken, and (b) the GW launch time corresponds to the GW launch height, which occurs a few minutes before the plume reaches $z > 50$ km. Thus we model primary GW launch times for these plumes of 04:17, 04:24, 04:34, 04:54, 05:14, and 05:44 UT. Note that the corresponding eruption times for the first four updrafts (which is estimated to be a few minutes before the GW launch times) roughly corresponds to the times estimated by Astafyeva et al. (2022, their Table 1) for the Main Explosion and Explosions 3–5, although we note that those times had uncertainties of ±2–5 min. We estimate plume updraft velocities of $w_{\rm pl} = 40$–120 m/s. Figure 2 shows these identified plumes used as input into MESORAC.

Figure 3 shows the background zonal wind $\overline{U}$, meridional wind $\overline{V}$ and temperature $\overline{T}$ taken from the HIAMCM base run near the location of the first plume. The wind from $z = 90$–300 km is northeastward, southward, then northward. Figures 4a–4c show the vertical wind perturbation, w', of the primary GWs from 4:58–6:30 UT at $z = 130$ km. At this altitude, the GWs are still mainly propagating upward and outward from Tonga. Large vertical winds up to ~200 m/s occur north and south of Tonga. Northward (southeastward)-propagating GWs reach the thermosphere earlier (somewhat later) due to their different wind filtering environments. We calculate the zonal and meridional local body forces (vertical flux of zonal and meridional momentum, respectively) as $F_x = -(\overline{\rho})^{-1}\partial\left(\overline{\rho}\,\overline{u'w'}\right)/\partial z$ and $F_y = -(\overline{\rho})^{-1}\partial\left(\overline{\rho}\,\overline{v'w'}\right)/\partial z$, respectively, where u' and v' are the zonal and meridional velocities of the primary GWs, $\overline{\rho}$ is the background density, and the overline denotes an average over the primary GW wavelength. Figures 4d–4i show the zonal and meridional local body forces at $z = 182$ km and 5:10–5:46 UT that result from the dissipation of primary GWs. At this altitude, most of the primary GWs have dissipated. Note that the forces in Figures 4d–4e and 4g–4h contain the momentum flux divergence from some of the primary GWs shown in Figures 4a and 4b, and are thus shown ~15 min later. Note that the delay of ~50–70 min from the primary GW launch times to the formation of the first body forces in the thermosphere occurs because it takes this amount of time for the primary GWs to propagate to $z \sim 180$ km (for example, Vadas & Liu, 2009). At 5:10 UT several northward body forces with amplitudes of ~0.65 m/s^2 are ~500 km north of the volcano. At 5:30 UT, a large-diameter southeastward body force with an amplitude of ~−2.2 m/s^2 is ~400 km southeast of the volcano. At 5:46 UT and later, the body forces are weaker due to the smaller updraft velocities. Due to

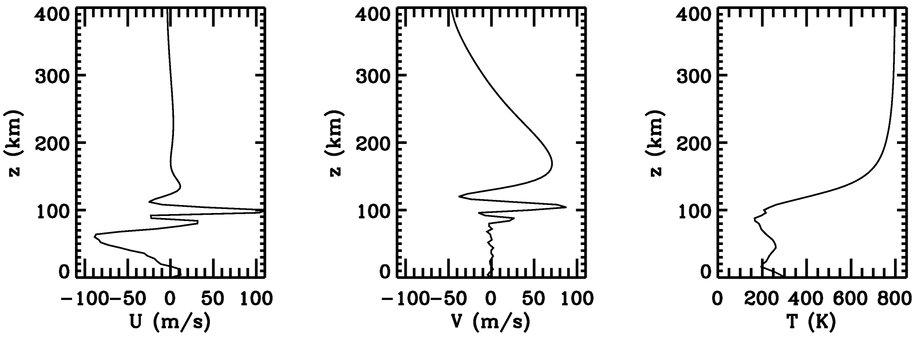

Figure 3. $\overline{U}$ (a), $\overline{V}$ (b) and $\overline{T}$ (c) from the HIgh Altitude Mechanistic general Circulation Model base run at 184.2°E, 20.67°S at 4:17 UT on 15 January 2022.

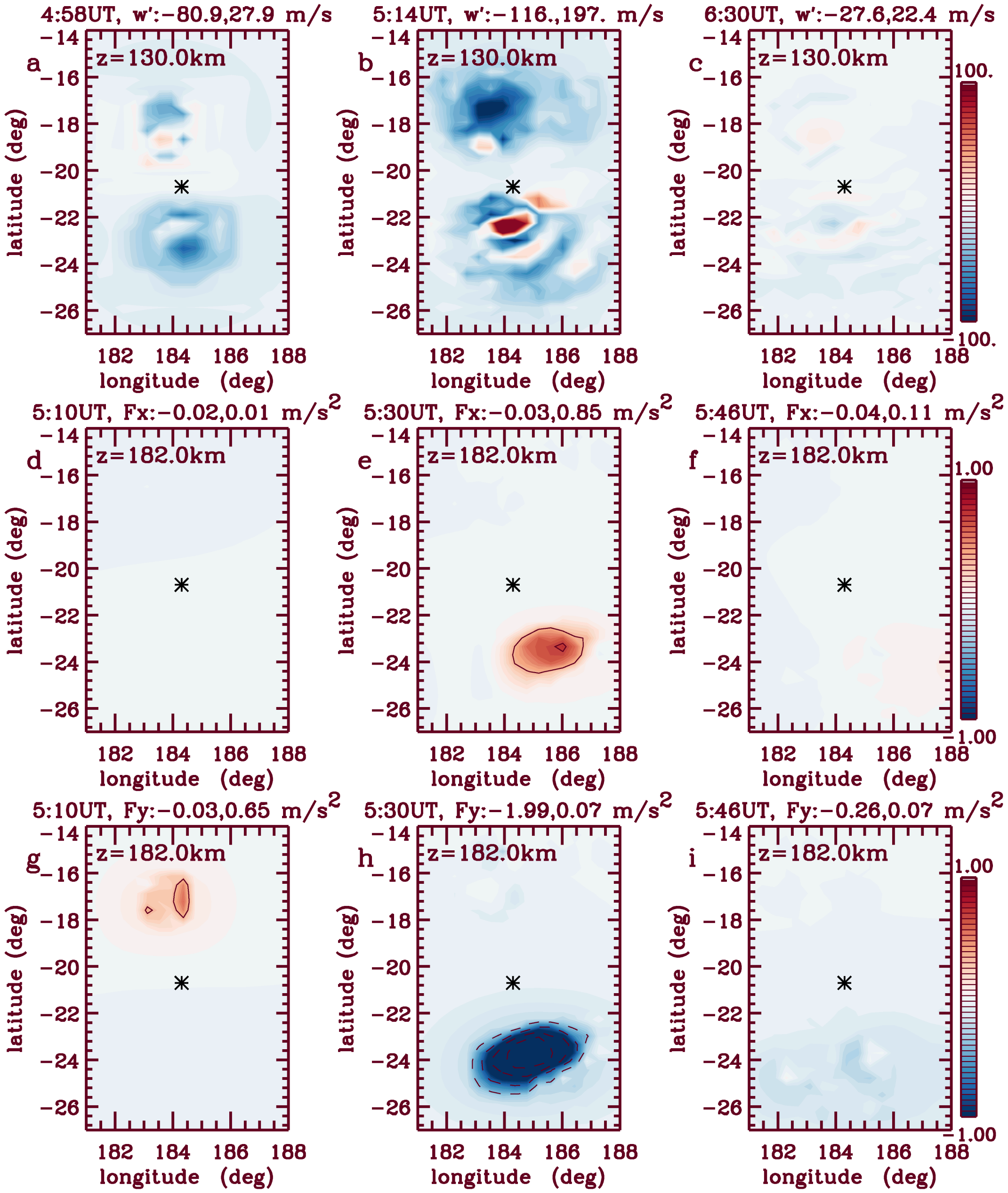

Figure 4. The vertical velocity perturbation w' from MESORAC due to the primary gravity waves (GWs) from Tonga at $z = 130$ km at 4:58, 5:14, and 6:30 UT (a–c) on 15 January 2022. The vertical flux of zonal momentum, F_x, from the dissipation of the primary GWs at $z = 182$ km at 5:10, 5:30, and 5:46 UT from MESORAC (d–f) on 15 January 2022. Solid (dashed) contour lines show positive (negative) values with a 0.4 m/s^2 interval. (g–i) Same as (d–f) but for the vertical flux of meridional momentum, F_y. Minimum and maximum values are given in each panel.

their large frequencies, the primary GWs propagate close to the zenith and therefore do not propagate farther than ~600 km horizontally from Tonga.

2.2. Model: Secondary GWs From Tonga

The HIAMCM is a high-resolution whole-atmosphere model for the neutral dynamics (Becker & Vadas, 2020). It employs a spectral dynamical core with a terrain-following hybrid vertical coordinate, a correction for non-hydrostatic dynamics, and consistent thermodynamics in the thermosphere. The current model version uses a triangular spectral truncation at a total wavenumber of 256, which corresponds to a horizontal grid spacing of ~52 km. The altitude-dependent vertical resolution includes 280 full levels. The highest model layer is located at $z \sim 400$–450 km, depending on the background temperature. The HIAMCM simulates GWs explicitly with an effective resolution that corresponds to a horizontal wavelength of $\lambda_H \sim 200$ km. Resolved GWs are dissipated self-consistently by molecular diffusion in the thermosphere above $z \sim 200$ km, and predominantly by macro-turbulent diffusion using the Smagorinsky-type diffusion scheme at lower altitudes. Topography and a simple ocean model, as well as radiative transfer, boundary layer processes, and the tropospheric moisture cycle are fully taken into account. The large scales of the model are nudged to Modern-Era Retrospective analysis for Research and Applications, Version 2 (MERRA-2) reanalysis in the troposphere and stratosphere, allowing for the simulation of observed events. A simple ion drag parameterization is included as the only ionospheric process included in the model. Further details of the HIAMCM are given in Becker, Goncharenko, et al. (2022) and Becker, Vadas, et al. (2022) and references therein.

We perform 2 HIAMCM runs here. The first is the "base run", which is the HIAMCM simulation on 15 January 2022 without the inputs from MESORAC. This is the run used as the background atmosphere for the ray tracing in the MESORAC model. The second HIAMCM simulation includes the inputs from MESORAC ("Tonga run") on 15 January 2022.

2.3. Data: Neutral Wind From MIGHTI Aboard the ICON Spacecraft

The National Aeronautics and Space Administration Ionospheric Connection Explorer (ICON) was launched into a 27° inclination orbit in 2019. Here, we use the neutral wind data from the MIGHTI instrument on the ICON spacecraft. Neutral wind profiles (ICON data product 2.2 v04) from $z = 90$–300 km are obtained from observations of green 557.7 nm and red 630.0 nm airglow emissions (Englert et al., 2017; Harding et al., 2017, 2021; Makela et al., 2021). Here we use the green (red) line measurements below (above) $z = 180$ km.

3. Secondary GWs Created by the Tonga Volcano

Figure 5 shows the zonal wind perturbation, $\Delta u = u - u_{\text{base}}$, computed from the HIAMCM run with the Tonga event minus the base run at $z = 200$ km every 2 hr from 6:00 to 20:00 UT. A continuum of medium to large-scale secondary GWs with concentric ring structure are seen radiating away from Tonga on global scales, with zonal wind perturbations as large as $u' \sim 200$ m/s. Here, we define medium and large-scale waves as having $100 \le \lambda_H < 1{,}000$ km and $\lambda_H \ge 1{,}000$ km, respectively (although note that the HIAMCM only has an effective resolution of $\lambda_H \ge 200$ km). Movie S1 shows the HIAMCM horizontal wind.

We overplot on Figure 5 equal distances from Tonga in 1,500 km intervals (dashed lines). The secondary GWs follow lines of equal distance as they propagate to the far side of the Earth. The secondary GWs have $\lambda_H \sim 400$–7,500 km, with λ_H increasing dramatically with radius $\mathcal{R}$ from Tonga; this is the expected result for GWs excited by a point source: $\lambda_H \propto \mathcal{R}^2$ at a given time t (Vadas & Azeem, 2021). The fastest secondary GWs, located at the largest radii at a given time t, have the largest λ_H; they follow the point source relationship $c_{IH} \propto \mathcal{R}$ at a given time t (Vadas & Azeem, 2021), where c_{IH} is the intrinsic horizontal phase speed. We also see that the largest values of λ_H increase in time as GWs with smaller vertical phase speeds and larger periods reach this altitude at larger $\mathcal{R}$. For example, at 6:00, 8:00, 10:00, and 12:00 UT, the GWs with the largest horizontal wavelengths are located at $\mathcal{R} = 2000$, 5,500, 9,000 and 12,000 km with $\lambda_H \sim 500$, 2,800, 5,500, and 7,500 km, respectively. Using $c_H = \lambda_H/\tau_r$ and assuming an approximate "earliest" generation time for the secondary GWs (from the body forces) of 5:00 UT, this implies propagation speeds of $c_H \sim 560$, 510, 500, and 476 m/s and wave periods of $\tau_r \sim 0.25$, 1.5, 3.1 and 4.4 hr, respectively. The fact that $\tau_r \ge 1$ hr for $\mathcal{R} > 5000$ km is not surprising, because GWs with large τ_{Ir} propagate large distances (horizontally) from a source, since $\cos\zeta \simeq \tau_B/\tau_{Ir}$ for GWs, where ζ is the propagation angle from the zenith, τ_{Ir} is the intrinsic period, and τ_B is the buoyancy period (for example, Vadas et al., 2009). Indeed, GWs created by a pinpoint source have $\tau_{Ir} \propto \mathcal{R}$ at a given time t (Vadas & Azeem, 2021).

The concentric ring structure in Figure 5 is asymmetric in that there is a significant decrease in the westward and eastward GW amplitudes as compared to the northwestward, southwestward, and southeastward amplitudes. This asymmetry can be seen at 8:00 UT over Australia and for the GWs propagating toward Central America. Such horizontal asymmetry is a standard feature of GWs generated by a local horizontal body force, since none of the radiated GWs propagate perpendicular to the force direction (Vadas et al., 2003, 2018). More specifically, four

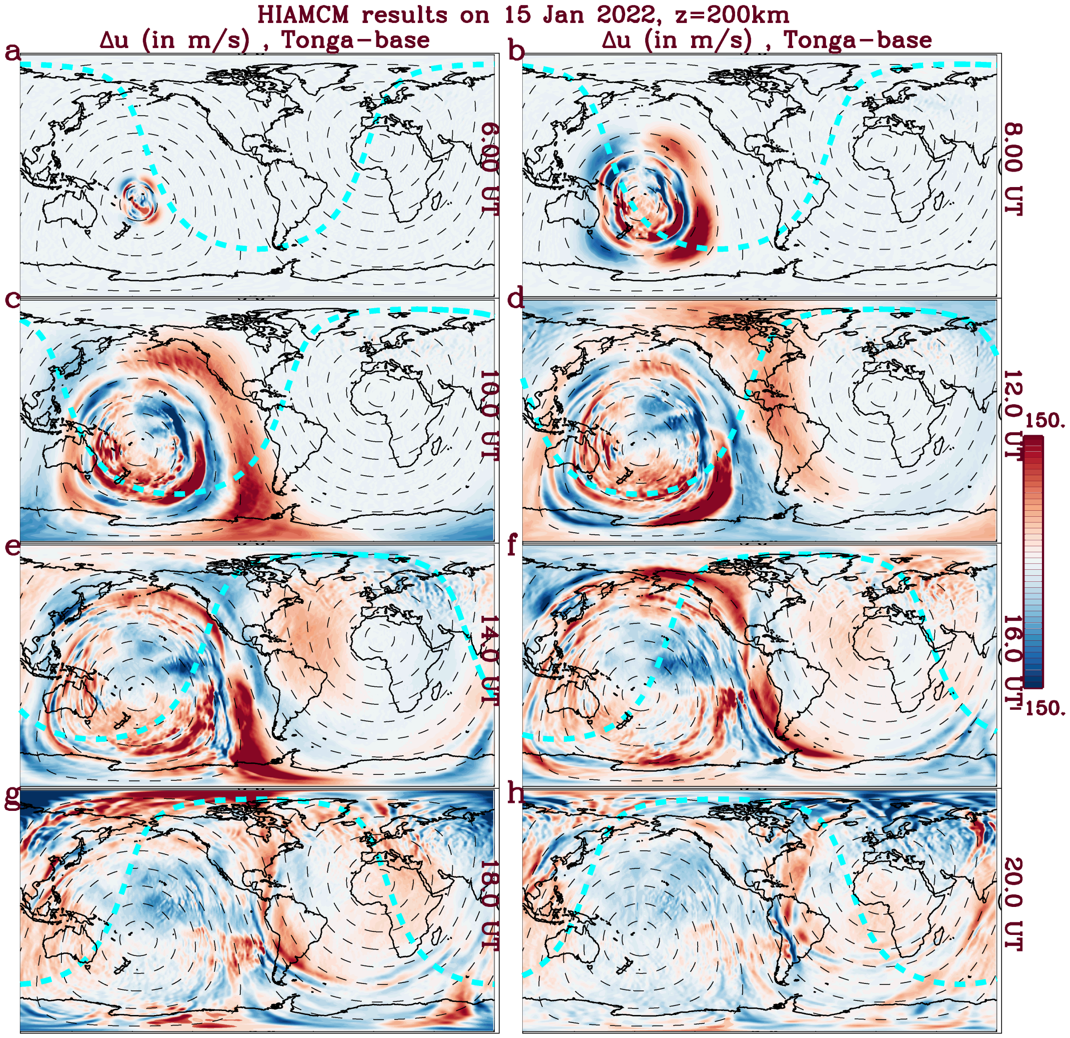

Figure 5. (a–h) HIgh Altitude Mechanistic general Circulation Model (HIAMCM) zonal wind response Δu (in m/s) at z = 200 km computed from the HIAMCM run with the Tonga event minus the base run every 2 hr from 6:00 to 20:00 UT, respectively, on 15 January 2022. The colors are oversaturated to emphasize the waves. The black dashed lines show equal distances from Tonga in 1500 km intervals. The turquoise dashed lines show the solar terminator.

cone-shaped "beams" of GWs are radiated from a local horizontal body force; these beams propagate forward/upward, forward/downward, backward/upward, and backward/downward along the force direction. Because of the asymmetry shown in Figure 5, we infer that the body forces were directed meridionally with a slight westward tilt. This agrees with the direction of the body forces in Figure 4, which were northward and southeastward due to the filtering of the background wind in the thermosphere, which was mainly directed in the meridional direction (see Figure 3). (Note that the regions north and south of Tonga where $\Delta u = 0$ in Figure 5 is not a reflection of an additional asymmetry.)

The first GWs reach New Zealand at ~6:00 UT with fast phase speeds in excess of 500 m/s, in reasonable agreement with observations (for example, Themens et al., 2022). The fastest GWs reach the western Continental United States (CONUS) at ~8:30–9:00 UT. These GWs are large-scale, $\lambda_H \sim$ 5,000–6,000 km, have large phase speeds of $c_H \sim 600$ m/s and large periods of $\tau_r \sim$ 2–3 hr. Since the sound speed is $c_s \sim 620$ m/s at this altitude, these secondary GWs propagate close to the sound speed; thus their simulation requires nonhydrostatic dynamics.

Figures 6a and 6b show latitude-height slices of the meridional wind perturbation Δv computed from the HIAMCM run with the Tonga event minus the base run at 185°E at 7:00 and 10:00 UT. North and southward secondary GWs having $|v'| \sim$ 100–200 m/s are seen propagating away from Tonga. The fastest GWs have the

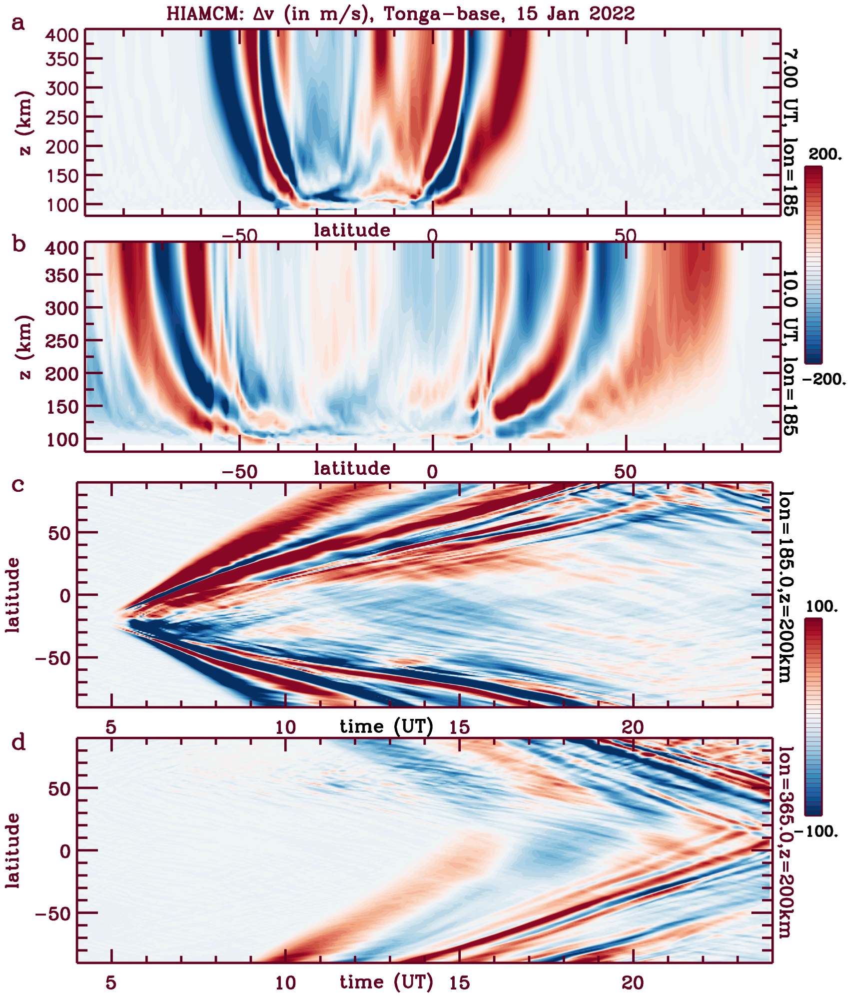

Figure 6. HIgh Altitude Mechanistic general Circulation Model (HIAMCM) meridional wind response Δv (in m/s) for the Tonga run minus the base run on 15 January 2022. (a–b) Vertical/latitude slices at 185°E at 7:00 and 10:00 UT, respectively. (c) Time/latitude slice at 185°E and $z = 200$ km. (d) Time/latitude slice at 365°E and $z = 200$ km. The colors are oversaturated to emphasize the waves of interest.

largest λ_H, while the medium-scale GWs propagate more slowly. Movie S2 shows the HIAMCM zonal wind Δu, meridional wind Δv, and vertical wind Δw perturbations (in m/s) computed from the Tonga run minus the base run at 21° S as a function of longitude and altitude (upper to lower panels, respectively).

Figure 6c shows Δv as functions of time and latitude at 185°E and $z = 200$ km, while Figure 6d shows the same keogram but at 365°E, thereby displaying the GWs which propagate to the far side of the Earth. The fastest secondary GWs are large-scale, and reach the antipode over Africa at ~16:00 UT (at 4°E and 19.5°N), or 9 hr after being created. Note that the slower medium-scale GWs have propagation speeds that are approximately 1/2 that of the fastest GWs and reach the antipode at 22:00–23:00 UT, 17–18 hr after creation. This implies that these latter GWs re-pass over Tonga ~36 hr after generation, in good agreement with Zhang et al. (2022).

Figure 7a shows Δv at $z = 200$ km and 185°E as functions of distance and time from Tonga, and Figure 7b shows a blow-up of Figure 7a for the region north of Tonga. Thermospheric GWs that originated above Tonga at 5:00 UT with propagation speeds of $c_H = 100$–600 m/s are overplotted. Here, $\Delta v = v - v_{\mathrm{base}}$ is computed from the HIAMCM run with the Tonga event minus the base run. Note that Δv changes/flips sign when the GWs propagate over the polar regions (to the far side of the Earth) in Figure 7a. For example, this occurs for the fastest northward secondary GWs at 12:00 UT and 20,000 km from Tonga. The secondary GWs span a wide range of scales: $\lambda_H \sim 400$–$7{,}500$ km, $c_H \sim 100$–600 m/s, and $\tau_r \sim 20$ min to 7 hr. The medium-scale GWs have $c_H \sim 100$–250 m/s, while the large-scale GWs have $c_H \sim 200$–600 m/s; thus the medium and large-scale GW meridional velocity

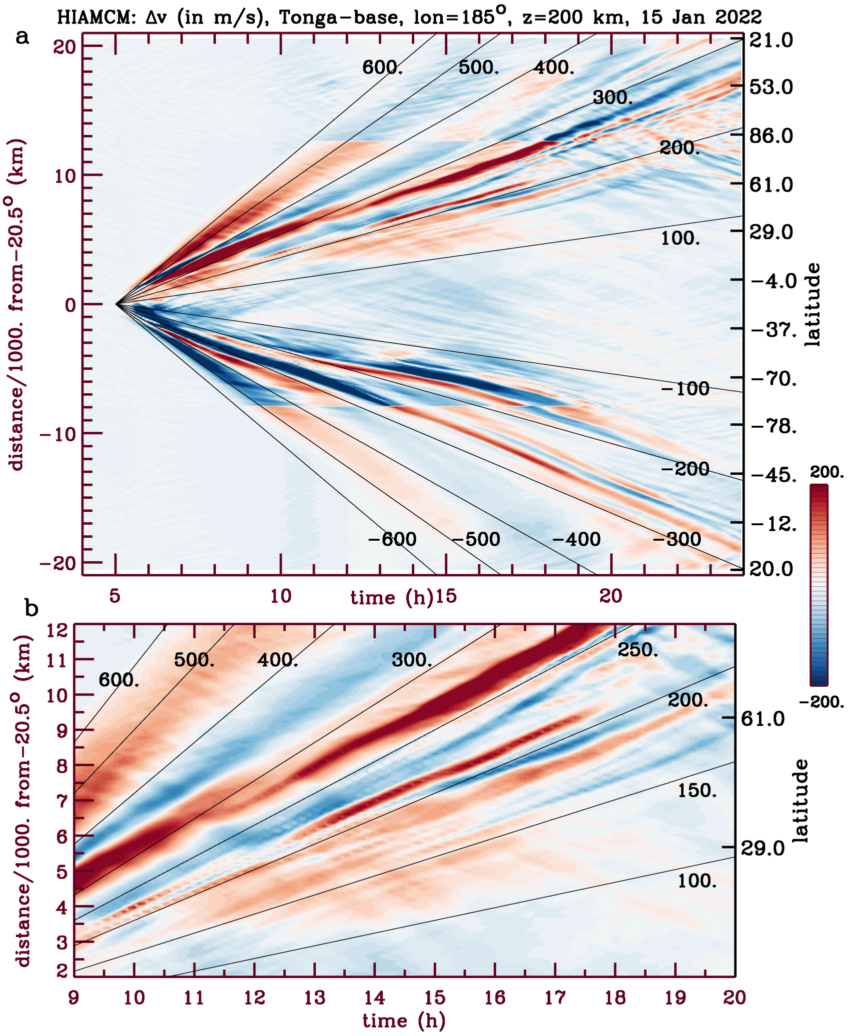

Figure 7. (a) Keogram of HIgh Altitude Mechanistic general Circulation Model (HIAMCM) Δv (in m/s) for the Tonga run minus the base run at 185°E and $z = 200$ km on 15 January 2022 as functions of the distance from Tonga and time. Solid lines show the propagation paths of thermospheric gravity waves (GWs) that originated above Tonga at 5:00 UT with meridional/horizontal phase speeds of $c_y = c_H = \pm 100$, 200, 300, 400, 500, and 600 m/s. Note that Δv changes/flips sign when the GWs propagate over the polar regions (to the far side of the Earth). (b) Blow-up of the upper part of (a) with an additional line at $c_H = 250$ m/s. The colors are oversaturated to emphasize the waves.

spectra overlap for horizontal phase speeds of $c_H \sim 200$–250 m/s. The GW amplitudes decrease in time because of wave dispersion, wave dissipation and geometric attenuation.

From Figure 7a, the GWs which reach $z = 200$ km at early times (5:00–8:00 UT) have $c_H \sim 600$ m/s and $\tau_r \sim 30$–40 min, and are located near Tonga, $\mathcal{R} \leq 5000$ km, in agreement with observations (for example, Themens et al., 2022). (This phase speed is also consistent with ICON observations of large-amplitude (>100 m/s) plasma drifts conjugate to the eruption's near-field within an hour of the eruption, for which the inferred driving neutral wind perturbations propagated at 600 ± 50 m/s (Gasque et al., 2022)). However by 13 UT, the fastest GWs which reach this altitude have somewhat slower speeds of $c_H \sim 500$ m/s, much larger periods of $\tau_r \sim 6$ hr, and are located far from Tonga: $\mathcal{R} = 10,000 - 12,000$ km. The fact that c_H is smaller at 13:00 UT is *not* due to the "slowing" of GWs, because these are *not* the same GWs that were seen at 5:00–8:00 UT close to Tonga. The fact that they are not the same GWs can be understood because a GW propagates horizontally *and* vertically at the "same time"; therefore, the GWs observed at 13:00 UT are "new" secondary GWs from below having slower vertical group velocities, larger λ_H, and larger τ_r.

In general, Figure 7 shows that the fastest GWs have $500 \le c_H \le 600$ m/s at $5000 \le \mathcal{R} \le 21,000$ km, but with λ_H and τ_r increasing dramatically with $\mathcal{R}$. Note that GWs with $100 \le c_H \le 500$ m/s are observed at all radii $\mathcal{R} \le 21,000$ km.

The discussion from the previous paragraphs (and Figure 7) explains why the GPS/TEC studies discussed in Section 1 observed GWs with $400 \le c_H \le 700$ m/s over New Zealand, but not over the CONUS at $\mathcal{R} \sim 9000 - 12000$ km; it was because they filtered out GWs with $\tau_r > 1$ hr, which limited their observations of the fastest secondary GWs with $c_H \sim$ 500–600 m/s to $\mathcal{R} \le 4000$ km (see also Section 6). We show in a companion paper that using a relaxed analysis constraint with $\tau_r \le 3$ hr and $\tau_r \le 2$ hr, GWs with $500 \le c_H \le 600$ m/s are observed over the CONUS and South America in GPS/TEC, respectively (Vadas et al., in preparation), in good agreement with our model results.

Figure 7b shows that the GWs with the largest amplitudes in the Northern Hemisphere are large-scale GWs, with $\lambda_H \sim$ 1,500–5,000 km, $c_H \sim$ 250–300 m/s and $\tau_r \sim$ 2.5–4 hr. The fact that these specific GWs have the largest amplitudes is because the body forces have diameters of $\mathcal{D} \sim 400$ km and are separated by ~900–1,000 km (see Figure 4), which excites secondary GWs having the largest amplitudes at $\lambda_H \sim$ 800–3,000 km (Vadas et al., 2003). The medium-scale GWs with $c_H \sim$ 200–250 m/s and $\tau_r \sim$ 20–60 min have relatively smaller amplitudes at $\mathcal{R} \ge 5000$ km. Because Lamb waves from the eruption have $\lambda_H \sim 150$ km and $\tau_r \sim 8$ min (Wright et al., 2022), none of these medium or large-scale secondary GWs could be caused by the leakage of lower atmospheric Lamb waves into thermospheric GWs (see Section 6).

4. Large to Global Scale Horizontal Wind Changes in the Thermosphere

We now examine the large to global-scale changes of the horizontal wind in the thermosphere caused by the secondary GWs from Tonga. The left column of Figure 8 shows the total horizontal wind perturbations, $\Delta u_H = \sqrt{\Delta u^2 + \Delta v^2}$, at $z = 200$ km computed from the Tonga run minus the base run for wave periods of $\tau_r > 5$ hr (using Fourier filtering). Wind differences include inertia GWs, tides and the terminator wave. The wind differences are highly variable spatially and temporally, have large amplitudes of ~80–120 m/s, and follow lines of equal distance from Tonga. These wind differences are due to (a) the dissipation of secondary GWs and subsequent change of the ambient flow, and (b) the wind components of propagating secondary GWs with $\tau_r > 5$ hr. The right column shows the horizontal wind from the base run. At this altitude, the large-scale horizontal wind is mainly due to the westward-propagating EUV-generated diurnal tide and the terminator waves (Forbes et al., 2008; Miyoshi et al., 2009). For example, a sunset terminator wave with $u'_H \sim 50 - 100$ m/s is seen at ~18:00 UT with a northwest/southeast phase front that stretches from the north Atlantic Ocean to northern Africa. A sunrise terminator wave with a northeast/southwest phase front is seen at the same time (i.e., at 18:00 UT) over the Pacific Ocean, although it has a smaller amplitude in the Northern Hemisphere than that of the sunset terminator wave at that time.

We can better understand the wave mean-flow interactions that give rise to these wind changes by comparing Figures 5 and 8. At 8:00 UT, the fastest northeastward-propagating secondary GWs are located over the mid to eastern Pacific Ocean, whereby the large-scale wind is northeastward with an amplitude of ~60 m/s; because the propagation direction of these fastest secondary GWs and the wind is in the same direction (i.e., northeastward), $|\lambda_z|$ for these GWs decreases which results in enhanced dissipation from both molecular and macro-turbulent viscosity. The momentum deposition accompanying this dissipation creates the ~30–50 m/s northeastward wind difference seen there. At 12:00 UT, new fast GWs from below dissipate over North, Central, and South America, thereby creating eastward and northeastward wind changes of ~80 m/s. The slower medium-scale GWs arrive a few hours later. The initially southeastward medium-scale secondary GWs from Tonga first propagate over Antarctica then propagate northeastward toward South America at 14:00 UT. Since the background wind is southwestward there, $|\lambda_z|$ increases for these waves, which enables them to propagate to this altitude before succumbing to viscosity; this dissipation creates a northeastward wind change of ~100–120 m/s. At 16:00–18:00 UT, later-arriving new medium-scale GWs dissipate over South America, thereby creating northeastward wind changes of ~80–100 m/s. Finally, the large-amplitude northwestward-propagating medium and large-scale secondary GWs with $c_H \sim$ 200–250 m/s and $\tau_r \sim$ 20 min to 2 hr dissipate over eastern Russia at 16:00–18:00 UT, thereby creating large northward to northwestward wind changes of ~100–120 m/s. Note that the fastest secondary GWs propagate within the large eastward wind component of the terminator wave over Africa at ~18:00 UT, which enhances the dissipation of these GWs and leads to eastward wind changes of ~25 m/s.

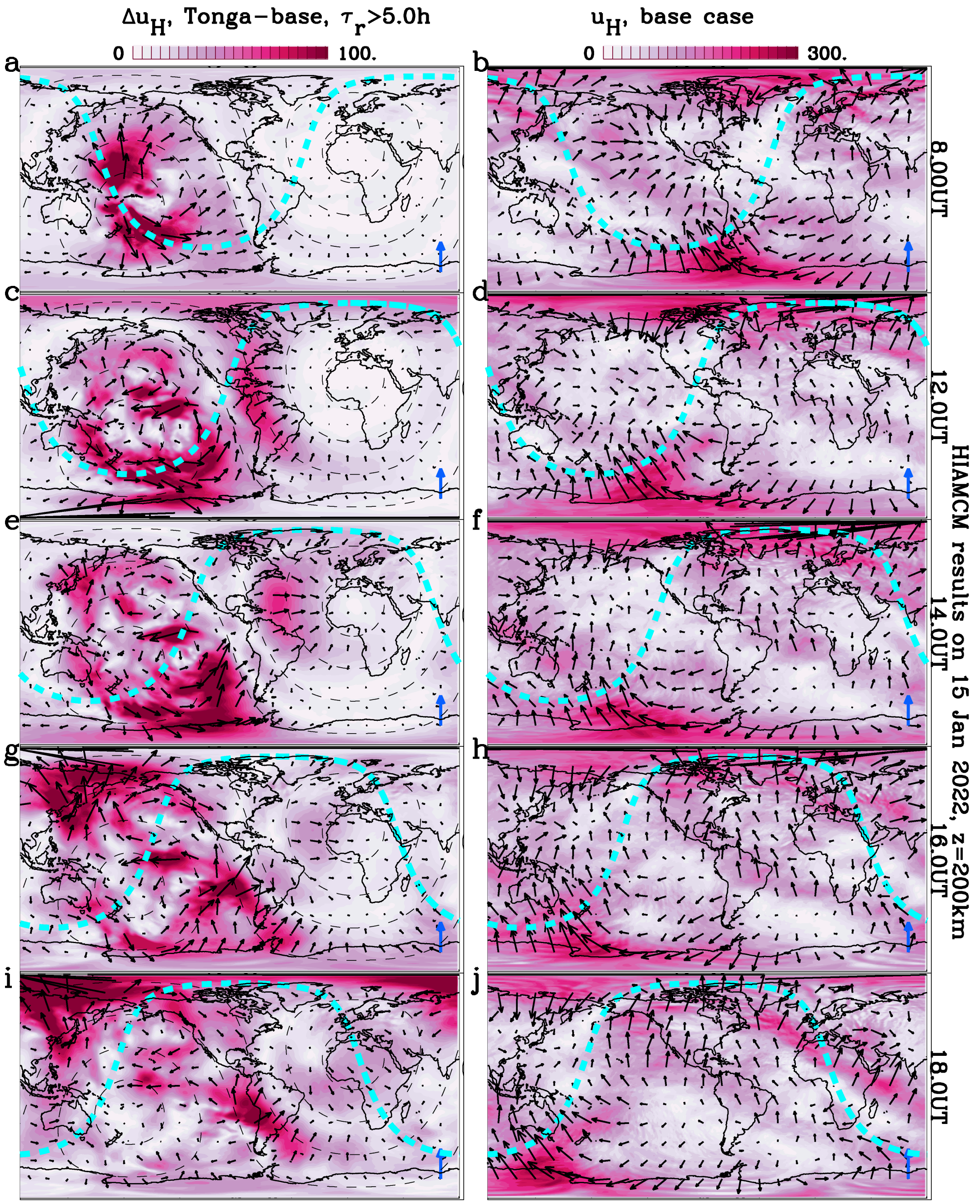

Figure 8. HIgh Altitude Mechanistic general Circulation Model (HIAMCM) horizontal wind on 15 January 2022 at $z = 200$ km. (a) Horizontal wind response, Δu_H (in m/s), for the Tonga run minus the base run for wave periods with $\tau_r > 5$ hr at 8:00 UT. The colors show the magnitude and the vectors show the direction. The black dashed lines show equal distances from Tonga in 3,000 km intervals. (b) Base horizontal wind (in m/s) at 8:00 UT. The colors show the magnitude and the vectors show the direction. Rows 2–5: Same as row 1 but for 12:00, 14:00, 16:00, and 18:00 UT, respectively. Note that the color scale for columns 1 and 2 is 100 and 300 m/s, respectively. The dark blue vectors show a northward wind of 100 m/s for reference. The turquoise dashed lines show the solar terminator.

5. Analysis of the Waves Observed by ICON and Comparison With the Modeled Waves

5.1. Analysis of the GWs Observed by ICON

Figure 9a shows the tangent longitude versus latitude (solid line, left y-axis) and the tangent longitude versus time (dashed line, right y-axis) for ICON orbit #12370. On this orbit, ICON-MIGHTI measured the neutral horizontal

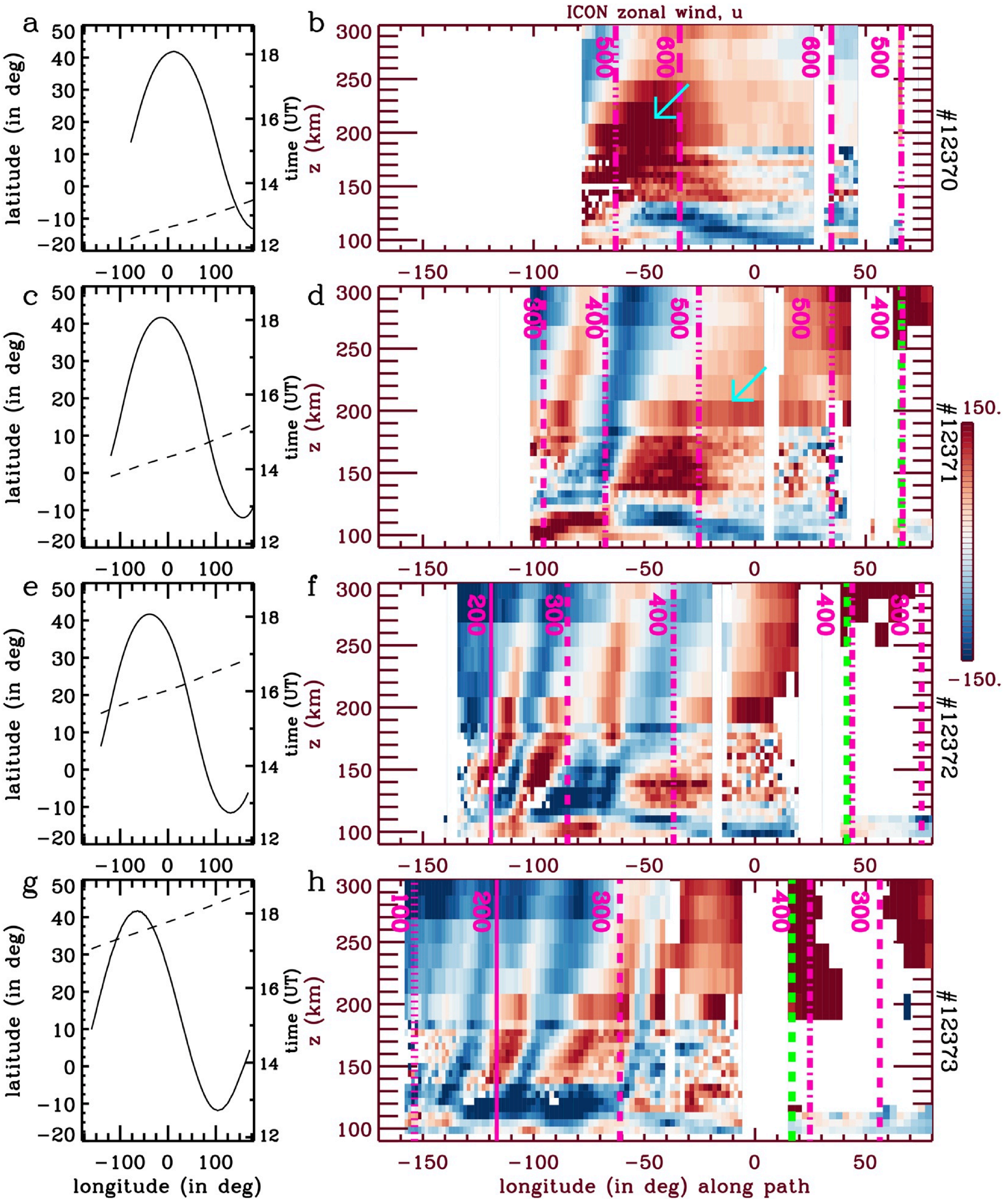

Figure 9. (a) ICON-MIGHTI tangent longitude versus latitude (solid line, left *y*-axis) and tangent longitude versus time (dashed line, right *y*-axis) for orbit #12370 on 15 January 2022. (b) ICON-MIGHTI zonal wind as functions of the tangent longitude and altitude for orbit #12370. Rows 2–4: Same as row 1 but for orbits #12371, 12372, and 12373. The pink dot, solid, dash, dash-dot, dash-dot-dot-dot, and long dash lines show the locations of thermospheric gravity waves (GWs) that originated above Tonga at 5:00 UT with $c_H = 100$, 200, 300, 400, 500, and 600 m/s, as labeled. c_H lines are not shown where the westward and eastward Tonga GWs overlap. Turquoise arrows indicate the fastest large-scale secondary GWs with $c_H \geq 500$ m/s. Green dash lines show the solar (sunset) terminator.

wind at ~12:00–13:30 UT on 15 January 2022. Figure 9b shows the observed zonal wind, u, at $z = 100$–300 km along the tangent longitude of this orbit. White patches indicate poor-quality ICON data. A large-scale, upward and eastward-propagating GW with $u' \sim 150$ m/s is observed at 12:30 UT at $140 < z < 250$ km at 10°–80°W and 30°N (i.e., over the mid-Atlantic Ocean), as indicated by the turquoise arrow. We overplot the propagation speeds of thermospheric GWs that originated above Tonga at 5:00 UT. The observed large-scale GW has a very fast propagation speed of $c_H = 500$–600 m/s. Comparing with the model results from Figures 5d and 5e, the location

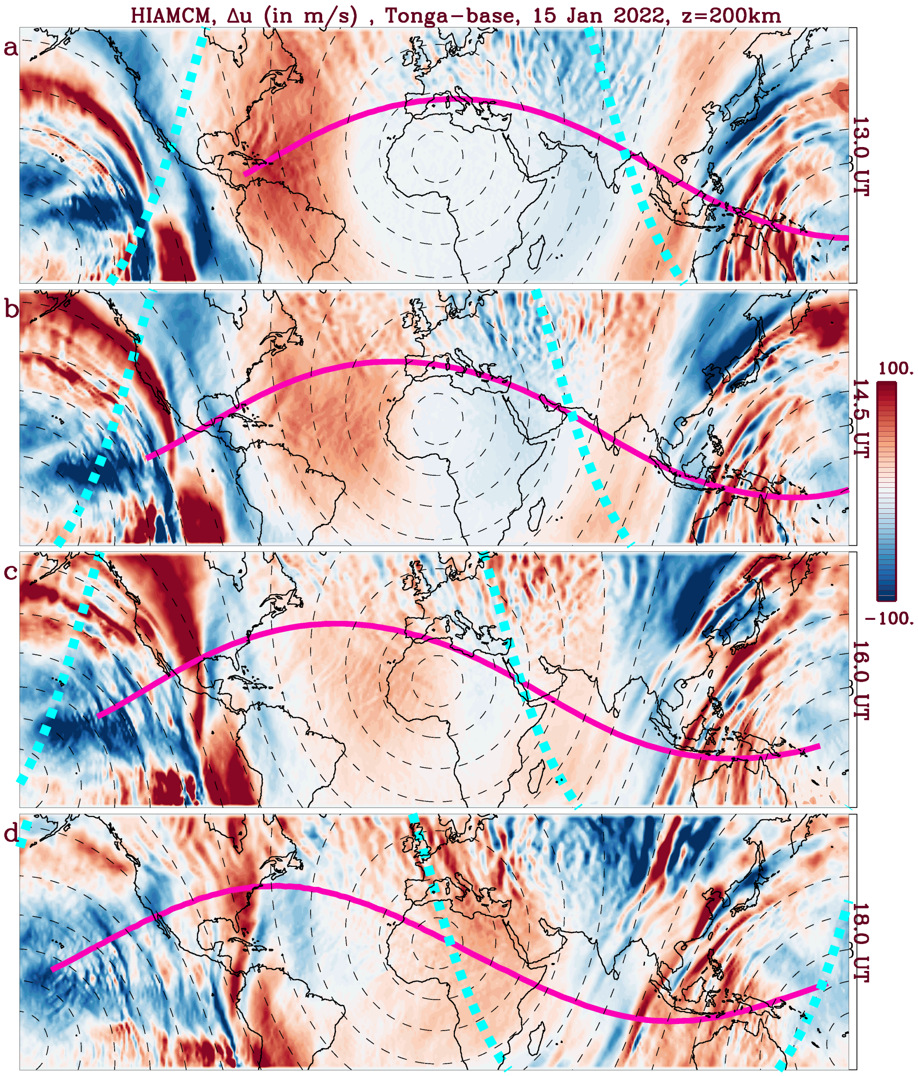

Figure 10. (a–d) HIgh Altitude Mechanistic general Circulation Model zonal wind response $\Delta u = u - u_{\text{base}}$ (Tonga run minus the base run) at 13:00, 14:30, 16:00, and 18:00 UT, respectively, on 15 January 2022 (colors, in m/s). We overlay ICON orbits #12370, 12371, 12372, and 12373 in (a–d), respectively, as pink solid lines. The black dashed lines show equal distances from Tonga in 1,500 km intervals. The turquoise dashed lines show the solar terminator. The colors are oversaturated to emphasize the waves.

and speed of this wave agrees well with that of the fastest large-scale secondary GWs from Tonga (i.e., over and just east of the Caribbean Sea).

Rows 2–4 of Figure 9 show the corresponding results for the next three successive orbits #12371, 12372, and 12373, which sample the atmosphere at ~13:45–15:15 UT, 15:30–17:00 UT, and 17:00–18:45 UT, respectively. (Note that Figures 9d and 9f show the same data as in Figures 1c and 1d of Harding et al., 2022.) Eastward and upward-propagating GWs are observed west of 0°E on the dayside. The along-track GW wavelength, λ_{track}, increases with distance from Tonga, as expected for GWs generated by a point source. In addition, the GWs in each successive orbit have smaller λ_{track} and smaller c_H at the same $\mathcal{R}$, in agreement with Figures 5d–5h and point-source theory. λ_{track} ranges from $\lambda_{\text{track}} \sim 800$ km for the GWs at the smallest $\mathcal{R}$ having $c_H \sim 100$ m/s (140°–170°W in Figure 9h) to $\lambda_{\text{track}} \sim 7{,}500$ km for the GWs at large $\mathcal{R}$ (70°W to 20°E in Figures 9b and 9d).

Figure 10 shows the HIAMCM Δu computed from the Tonga run minus the base run over the region spanning ICON orbits #12370–12373 at the approximate average orbit times of 13:00, 14:30, 16:00, and 18:00 UT. We overplot ICON orbits #12370, 12371, 12372, and 12373 in Figures 10a–10d, respectively. ICON sampled the fastest GWs from Tonga with c_H = 500–600 m/s over the Caribbean Sea and Atlantic Ocean during orbits #12370–12371, and sampled the slowest GWs with $c_H \simeq$ 100 m/s near Hawaii at the beginning of orbit #12373.

An important point from Figure 10 is that ICON sampled the northeastward-propagating secondary GWs from Tonga west of 0°E, and the northwestward-propagating secondary GWs east of 0° E. On each successive orbit, the northeast and northwestward GWs move closer together, with the fastest large-scale GWs interfering at 16:00 UT over northern Africa. Orbit #12370 sampled the fastest, largest-scale northeastward GWs over the Caribbean Sea and Atlantic Ocean, and the northwestward GWs over India and Thailand. It also sampled the slower medium to large-scale northwestward GWs over the southwestern Pacific Ocean. Orbits #12372–12373 sampled the slower medium to large-scale northeastward GWs over the Pacific Ocean and northwestward GWs over the Indian Ocean and Indonesia. Because of the westward progression of ICON for each successive orbit, ICON sampled most of the northeastward secondary GWs from Tonga during these four orbits. Because ICON fortuitously moved parallel to the GW propagation direction, $\lambda_H \simeq \lambda_{\text{track}}$ for these GWs.

Because ICON would have observed the northwestward-propagating GWs from Tonga east of 0°E, we include the horizontal phase speeds for these GWs in Figures 9b, 9d, 9f, and 9h. This is why there are multiple contour lines for the same values of c_H. (See, e.g., the multiple lines for c_H = 400 and 500 m/s in Figure 9d.) The fastest northeastward and northwestward Tonga GWs with c_H = 500 and 600 m/s interfere at ∼4°E during orbits #12371 and 12372, respectively. (Note that c_H contours are not shown in Figure 9 where the northwestward and northeastward GWs interfere.) Unfortunately, however, the ICON-MIGHTI data quality is poor where the northwestward GWs would have been observed because of the dimmer airglow emission at night. Therefore, we are unable to verify the presence of the northwestward-propagating GWs from Tonga in the ICON data in Figure 9.

In summary, Figures 9 and 10 show that ICON-MIGHTI observed northeastward-propagating GWs from Tonga with $100 \leq c_H \leq 600$ m/s and $\lambda_H \simeq$ 800–7,500 km, in good agreement with the model results (see Figures 5–7). Thus, these observations provide excellent confirmation of the body force generation mechanism for these secondary GWs from the Tonga eruption.

5.2. Comparison of the Observed and Modeled GWs and Tides

Figure 11a shows the zonal wind, u, measured by ICON as functions of the tangent longitude along orbit # 12372 and altitude. We now compare the observed wind with the HIAMCM zonal wind. We have found that the amplitudes of the HIAMCM Tonga GWs are typically ∼50% smaller than the observed GWs, especially for the fastest GWs. This underestimation is likely because the turbulent diffusion coefficient D_0 needed to be somewhat too large in MESORAC to keep the HIAMCM Tonga run from becoming unstable. For this reason, we artificially increase the amplitudes of the HIAMCM Tonga GWs by 50% and 150% in the following panels. In addition, the HIAMCM Tonga GWs are typically 0.5–1 hr behind the observed GWs. This is especially true for the fastest GWs, which have slightly smaller horizontal phase speeds than the observed values. These smaller values may have occurred because the sound speed in the thermosphere was somewhat smaller in the HIAMCM than in the real atmosphere, which can occur if the HIAMCM background temperature is a little smaller than the actual background temperature. (Note that the large-scale temperature in the HIAMCM is not nudged to the background atmosphere in the thermosphere due to a lack of data and/or realistic model.) For this reason, we sample the model results along ICON's tangent path 0.5 and 1.5 hr later in the following panels.

Figure 11b shows the HIAMCM $u_{\text{base}} + 1.5\Delta u$ sampled $\Delta t = 0.5$ hr later than the ICON times along orbit # 12372, where $\Delta u = u - u_{\text{base}}$. Since u_{base} contains the tides and terminator waves, we have effectively increased the HIAMCM Tonga GW amplitudes (but not the amplitudes of the tides and terminator wave) by 50% in this panel. Turquoise and pink arrows indicate the Tonga GWs and tides, respectively. Note that the locations of the tides and terminator waves are determined by plotting u_{base} separately (shown later). Here, the HIAMCM wind is smoothed zonally and meridionally over 200 km (before sampling the wind along the ICON tangent path) to simulate the horizontal averaging inherent in ICON-MIGHTI observations. Northeastward GWs are seen propagating away from Tonga, with horizontal wavelengths increasing with distance from Tonga, as expected for GWs created by a point source. These GWs propagate to z = 300 km. Figure 11c shows the same as Figure 11b, but for a 150% increase in the Tonga GW amplitudes. Upon comparing Figures 11b and 11c with Figure 11a, we estimate that the HIAMCM Tonga GW amplitudes are approximately two times smaller than the observed amplitudes. Figures 11d and 11e show the same results as in Figures 11b and 11c, but sampled $\Delta t = 1.5$ hr later

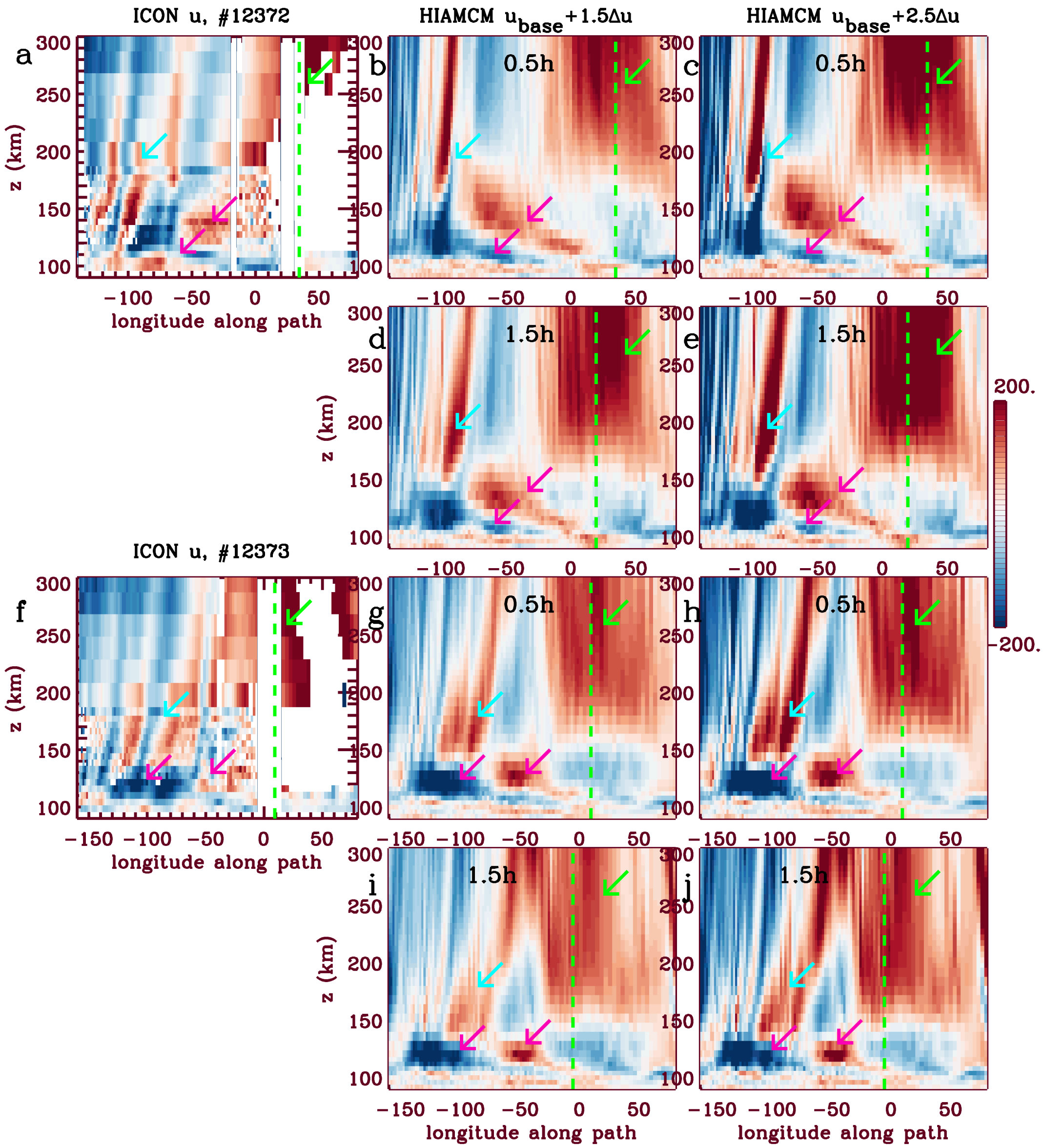

Figure 11. (a) ICON zonal wind as functions of the tangent longitude and z for orbit # 12372. (b) HIgh Altitude Mechanistic general Circulation Model (HIAMCM) $u_{\text{base}} + 1.5\Delta u$ as functions of the tangent longitude and z sampled $\Delta t = 0.5$ hr later than the ICON times for orbit # 12372. Here, $\Delta u = u - u_{\text{base}}$ (Tonga run minus base run). The HIAMCM winds are smoothed over 200 km horizontally prior to sampling. (c) HIAMCM $u_{\text{base}} + 2.5\Delta u$ sampled $\Delta t = 0.5$ hr later than the ICON times. (d–e) Same as (b–c) but sampled $\Delta t = 1.5$ hr later. (f–j) Same as (a–e) but for orbit # 12373. Green dashed lines indicate the sunset solar terminator. Turquoise, pink, and green arrows indicate the Tonga gravity waves, tides, and terminator waves, respectively, and are in the same locations in (a–e) and in (f–j).

than ICON. Upon comparing Figures 11b–11e with Figure 11a, we estimate that the HIAMCM Tonga GWs are ∼0.5 hr behind the observed GWs. Figures 11f–11j show the same observation and modeling results as in Figures 11a–11e but for orbit # 12373. In general, the timing, location, amplitudes, and wavelengths of the HIAMCM Tonga GWs agree reasonably well with the observed GWs, provided we multiply the GW amplitudes by ∼2 and sample the HIAMCM results ∼30 min later than ICON. This agreement is especially good for $z \geq 140$ km. Below $z < 140$ km, the HIAMCM Tonga GW amplitudes are significantly smaller than the observed values. Note that the location, amplitude, and timing of the zonal wind component of the tides (Figures 11b–11e and 11g–11j) agree reasonably well with the observed zonal wind (Figures 11a and 11f) at $z \leq 150$ km.

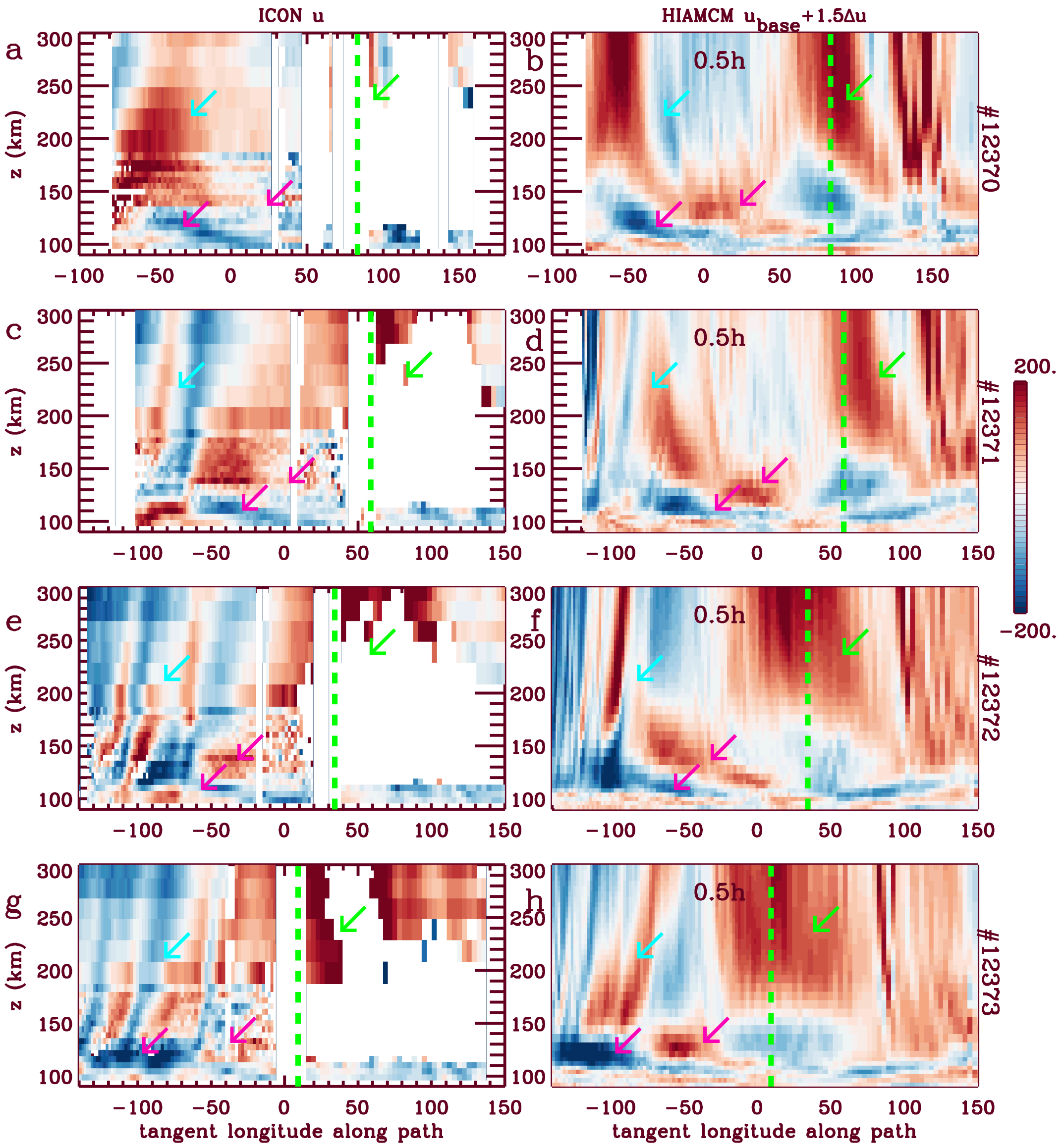

Figure 12. (a, c, e, g) Zonal wind measured by ICON as functions of the tangent longitude and z for orbits #12370, 12371, 12372, and 12373, respectively. (b, d, f, h) HIgh Altitude Mechanistic general Circulation Model (HIAMCM) $u_{\text{base}} + 1.5\Delta u$ as functions of the tangent longitude and z sampled $\Delta t = 0.5$ hr later than the ICON times for orbits #12370, 12371, 12372, and 12373, respectively. The HIAMCM winds are smoothed over 200 km horizontally prior to sampling. The green dashed lines show the sunset solar terminator. Turquoise, pink, and green arrows indicate the Tonga gravity waves, tides, and terminator waves, respectively, and are in the same locations in each row.

The solar terminator is shown in Figure 11 as a dashed green line. A feature consistent with the sunset solar terminator wave is that it is located at and just east of the solar terminator at these latitudes (green arrows), with large amplitudes of $u' \sim 200$ m/s. This terminator wave moves westward and has a width of a few thousand km. The western edge of the solar terminator wave is observed by ICON, although unfortunately the ICON data quality is poor at 50°–100°E at most altitudes. Where there is good data, however, the amplitude and location of the terminator wave in the HIAMCM agrees reasonably well with that observed by ICON. Further ICON-HIAMCM comparisons on other days are needed to confirm the large solar terminator wave seen in the model, an effort that is outside the scope of this study. Note that the Tonga GWs that propagate northwestward in Figure 10 are not visible in Figure 11 because they are overshadowed by the terminator wave.

The first column of Figure 12 shows the zonal wind measured by ICON-MIGHTI during orbits #12370, 12371, 12372, and 12373. The second column shows the HIAMCM $u_{\text{base}} + 1.5\Delta u$ sampled $\Delta t = 0.5$ hr later than ICON.

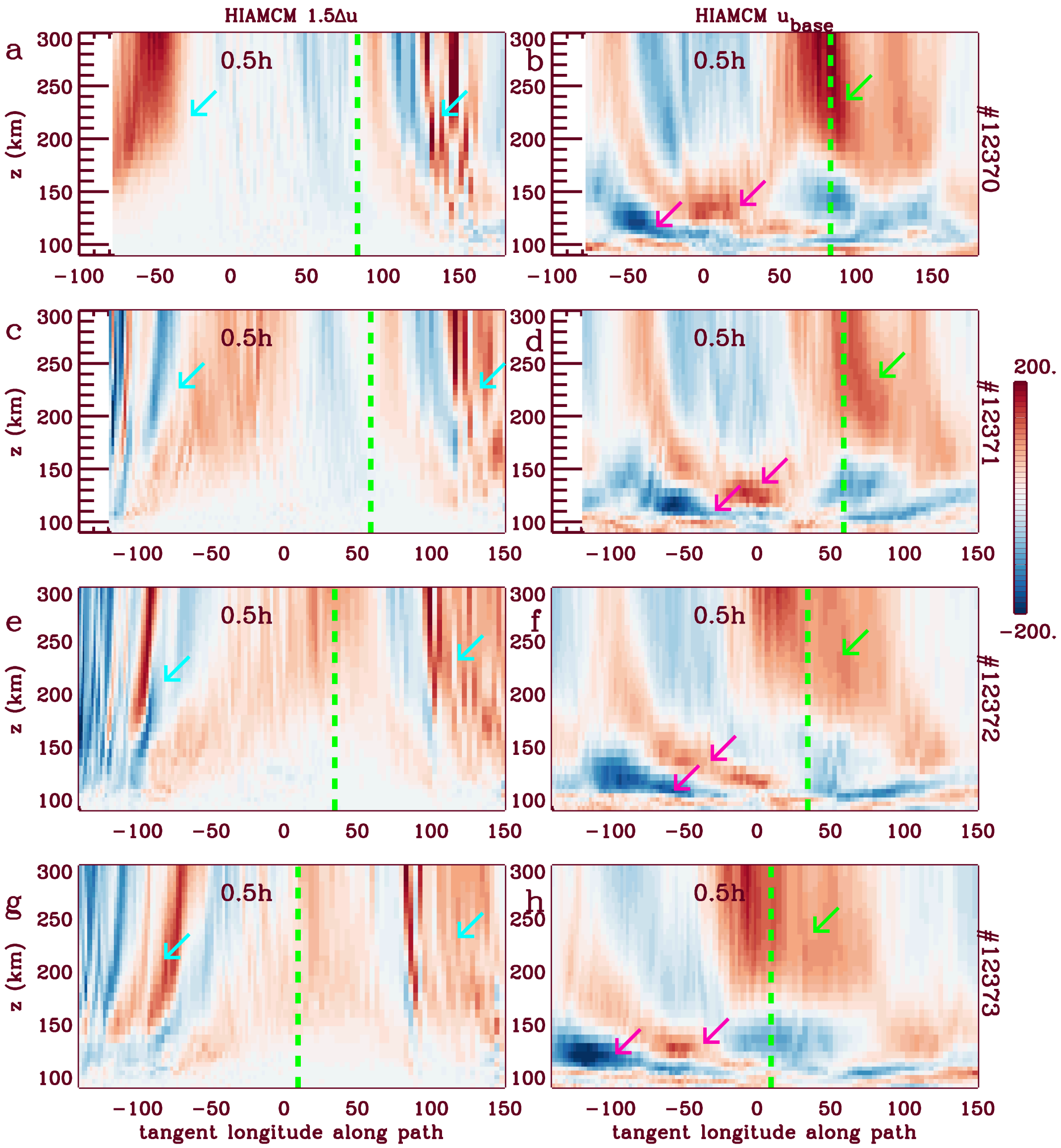

Figure 13. (a, c, e, g) HIgh Altitude Mechanistic general Circulation Model (HIAMCM) $1.5\Delta u$ as functions of the tangent longitude and z sampled $\Delta t = 0.5$ hr later than the ICON times for orbits #12370, 12371, 12372, and 12373, respectively. (b, d, f, h) Same as (a, c, e, g) but for the base run u_{base}. The HIAMCM winds are smoothed over 200 km horizontally prior to sampling. The green dashed lines show the sunset solar terminator. Turquoise arrows indicate the Tonga gravity waves (left column). Pink and green arrows indicate the tides and terminator waves, respectively (right column).

The first and second columns of Figure 13 shows the HIAMCM $1.5\Delta u$ and u_{base} sampled $\Delta t = 0.5$ hr later than ICON. Turquoise, pink, and green arrows indicate the Tonga GWs, the tides, and the terminator waves, respectively. The fastest, northeastward, large-scale GW observed by ICON during orbit #12370 at 0°–100°W is seen in the HIAMCM results at a similar location, although the HIAMCM GW has a different shape in longitude and altitude. In particular, while the observed GW dissipates at $z \sim 225$–275 km, the HIAMCM GW does not appear to dissipate below $z \sim 300$ km. The medium to large-scale GWs observed by ICON during orbits # 12371–12373 are also seen in the HIAMCM results at similar locations, with similar dependencies of λ_H on $\mathcal{R}$. In general, the timing, location and wavelengths of the HIAMCM GWs at 0°–180°W agree well with the ICON GWs, provided we multiply the GW amplitudes by 2 and sample the HIAMCM results ~30 min later than ICON-MIGHTI.

Comparing the HIAMCM tides in u_{base} with those observed by ICON, we see that the location, tilt and amplitude of the tides agree reasonably well with the tides observed by ICON at $z < 150$ km.

6. Discussion

Wright et al. (2022) observed a Lamb wave from Tonga in the troposphere and stratosphere. This wave propagated three times around the Earth, with a horizontal phase speed of $c_H \sim 300$–320 m/s. A Lamb wave is a special type of acoustic wave with zero vertical wavenumber, $m \sim 0$, which propagates at the sound speed c_s in the horizontal direction only (Gossard & Hooke, 1975).

The Lamb wave observed by Wright et al. (2022, their Extended Data in Figure 5) had $\lambda_H \sim 150$ km. We estimate a Lamb wave period of $\tau_r = \lambda_H / c_s \sim 8.1$ min. Lamb waves are created by phenomena such as volcanic eruptions, meteor impacts, nuclear testing, and earthquakes, and are typically concentrated in the troposphere because their energy decays exponentially in altitude (Nishida et al., 2013; Wright et al., 2022, and refs. therein). A Lamb wave can leak into the thermosphere and propagate thereafter as a GW at a resonant frequency of 3.5 mHz, which corresponds to $\tau_r \sim 4.8$ min (Nishida et al., 2013).

If a GW from Tonga has $c_H \sim 310$ m/s in the thermosphere, this does not imply that this GW is created from the leakage of a Lamb wave, *unless* it has a similar value of τ_r and λ_H as the stratospheric Lamb wave. Lin et al. (2022) and Zhang et al. (2022) suggested that the MSTIDs they observed in GPS/TEC with $c_H \sim 320$–390 m/s and $c_H \sim 350$ m/s, respectively, at $\mathcal{R} \geq 4000$ km were created by the leakage of a Lamb wave into the thermosphere. However, those MSTIDs had $\lambda_H \geq 400$ km, which does not agree with the measured horizontal wavelength of the Lamb wave in the stratosphere of $\lambda_H \sim 150$ km. In addition, Themens et al. (2022) noted that their far-field MSTIDs were consistent with the Lamb waves in their model. The reason these three studies mainly observed GWs with $c_H \sim 350$ m/s at $\mathcal{R} \geq 4000$ km was because they restricted their analyses methods to $\tau_r < 30$–50 min: Lin et al. (2022) only analyzed the $\tau_r \sim 12$–20 and 30–50 min waves using a Butterworth filter, Zhang et al. (2022) subtracted a 30 min sliding window data from the GPS/TEC data and so only analyzed waves with $\tau_r = 10$–30 min, and Themens et al. (2022) subtracted a 30 min boxcar smoothed data from the GPS/TEC data. As we found in this paper, it is precisely the $\tau_r > 1$ hr secondary GWs that reach the F region at large radii $\mathcal{R} \geq 4000$ km with horizontal phase speeds of $c_H \sim 500$–600 m/s.

Themens et al. (2022) were aware of this limitation, and stated "Use a detrending window that is too wide and you risk introducing substantial trends from quiescent ionospheric variability and masking smaller scale structures behind stronger large-scale variability. Use a detrending window that is too narrow and you risk removing parts of the desired signal. … Using the 30 min window will allow us to easily identify the MSTIDs, but may artificially suppress the observed amplitude of LSTID structures."

Harding et al. (2022) also suggested that the large-amplitude Tonga GWs observed by ICON were due to the leakage of the Lamb wave into thermospheric GWs; this suggestion was made because some of the GWs in orbits #12371 and 12372 had similar horizontal phase speeds as that of the Lamb wave in the stratosphere, even though λ_H was much greater than that of the Lamb wave. In fact, as we found in this paper, ICON observed GWs from Tonga with $c_H \sim 100$–600 m/s and $\lambda_H \sim 800$–$7{,}500$ km, in good agreement with the modeled secondary GWs from Tonga.

Based on the similarity of our model results with these observations, it is highly likely that the far-field MSTIDs from Tonga with $c_H \sim 320$–390 m/s reported by Lin et al. (2022), Themens et al. (2022), and Zhang et al. (2022) were nearly entirely medium to high-frequency secondary GWs excited by the body forces/heatings created from the dissipation of primary GWs created by Tonga, and were not due to the leakage of Lamb waves into thermospheric GWs.

7. Conclusions

In this paper, we modeled the excitation of primary and secondary GWs from the mechanical updrafts created by the Hunga Tonga-Hunga Ha'apai volcanic eruption on 15 January 2022. We used the MESORAC model suite to excite and propagate the primary GWs excited by the mechanical displacement of air from 4:15–5:50 UT that was caused directly by the eruption, not the primary GWs that were excited by the deep convection that ensued from the injection of water into the troposphere and stratosphere. We used the HIAMCM model to calculate the secondary GWs and mean wind effects created where the primary GWs dissipated. We found that the mechanically generated primary GWs propagated up to ∼600 km horizontally from the volcano before breaking and/or dissipating from molecular viscosity. Upon dissipating, they created local body forces and heatings. We added these forces and heatings to the HIAMCM, and found that they generated a continuum of medium to large-scale secondary GWs with $\tau_r \sim 20$ min to 7 hr, $\lambda_H \sim 400$–7,500 km, $c_H \sim 100$–600 m/s, and u', $v' \sim 100$–200 m/s. We found that the fastest secondary GWs with $c_H \sim 500$–600 m/s had the largest scales of $\lambda_H \sim 3{,}000$–7,500 km and the largest periods of $\tau_r \sim 1.5$–7 hr. These GWs reached the western US at ∼ 8:30 UT, and reached the antipode over Africa ∼9 hr after generation. The medium-scale secondary GWs were significantly slower, with $c_H \sim 100$–250 m/s, $\lambda_H \sim 400$–1,000 km and $\tau_r \sim 20$–60 min. Tonga also generated slower, large-scale secondary GWs with $200 \le c_H \le 400$ m/s. Those secondary GWs with $c_H \sim 350$ m/s reached the antipode after ∼18 hr, in agreement with Zhang et al. (2022). We also found that the large-scale horizontal wind in the thermosphere changed by ∼80–120 m/s over temporally and spatially localized regions globally due to the dissipation of medium and large-scale secondary GWs.

We then analyzed the ICON-MIGHTI zonal wind measurements. We found that ICON observed the fastest, largest-scale GWs with $c_H \sim 500$–600 m/s during orbits #12370–12371. For the four orbits we analyzed (#12370–12373), ICON observed northeastward-propagating GWs with $c_H \sim 100$–600 m/s and $\lambda_H \sim 800$–7,500 km, in good agreement with our model results. In addition, we found that the timing, location, amplitudes, and wavelengths of the ICON Tonga GWs agreed well with the modeled secondary GWs, provided we increased our modeled GW amplitudes by a factor of ∼2 and sampled our results ∼30 min later than ICON. Note that none of the thermospheric GWs with $c_H \ge 300$ m/s could have been generated below $z < 80$–100 km because the maximum value of c_{IH} a GW can have in the lower and middle atmosphere is $c_{IH} = 0.9c_s$ (Equation 36 of Vadas et al., 2019), where c_s is the sound speed and c_{IH} is the intrinsic horizontal phase speed. At $z < 110$ km, $c_s = 280$–310 m/s.

We also found that the zonal wind components of the westward migrating tides in the HIAMCM agreed reasonably well with the tides observed by ICON at $z \le 150$ km. Finally, we found that the onset of the sunset terminator wave created by the HIAMCM agreed reasonably well with that in the ICON data, although the ICON data quality was generally poor at $z < 250$ km when sampling the sunset terminator wave because of the dimmer airglow emission at night.

In conclusion, we found that ICON-MIGHTI observed the medium to large-scale secondary GWs from Tonga with $c_H \sim 100$–600 m/s and $\lambda_H \sim 800$–7,500 km, thereby providing strong confirmation of the modeled secondary GWs and the body force generation mechanism. A companion paper inputted the HIAMCM neutral wind into SAMI3. They found that the Tonga event created a "super" equatorial plasma bubble that extended ∼30° in longitude and up to 500 km in altitude, and had a density depletion of three orders of magnitude (Huba et al., 2023).

Data Availability Statement

ICON data can be retrieved from the ICON website (https://icon.ssl.berkeley.edu/Data). MERRA-2 reanalysis data was used to nudge the HIAMCM, and is available for download at https://gmao.gsfc.nasa.gov/reanalysis/MERRA-2/data_access/. GOES-17 data can be retrieved from the NOAA Comprehensive Large Array-Data Stewardship System (CLASS) at https://www.avl.class.noaa.gov/saa/products/welcome. The model data shown in this paper will be available at the time of publication at https://www.cora.nwra.com/vadas/Vadas-etal-JGR-2023-TongaICON-files/. https://icon.ssl.berkeley.edu/Data). (https://icon.ssl.berkeley.edu/Data). MERRA-2 reanalysis data was used to nudge the HIAMCM, and is available for download at https://gmao.gsfc.nasa.gov/reanalysis/MERRA-2/data_access/. GOES-17 data can be retrieved from the NOAA Comprehensive Large Array-Data Stewardship System (CLASS) at https://www.avl.class.noaa.gov/saa/products/welcome. The model data shown in this paper will be available at the time of publication at https://www.cora.nwra.com/vadas/Vadas-etal-JGR-2023-TongaICON-files/.

Acknowledgments

The authors would like to thank an anonymous reviewer for helpful comments, and Neil Hindley for helpful discussions. S.L.V. and E.B. were supported by NASA Grants 80NSSC19K0836, 80NSSC20K0628, and 80NSSC22K0174. S.L.V. was also supported by NSF Grants AGS-1822867 and AGS-1832988. E.B. was additionally supported by the Leibniz Institute of Atmospheric Physics at the University of Rostock (IAP), which partly provided the HPC facility used for this study. C.F. was supported by Fundação de Amparo à Pesquisa do Estado de São Paulo (FAPESP) under grants 2018/09066-8 and 2019/22548-4. KB was supported by NASA Grant 80NSSC19K0836. B.J.H. and L.C.G. were supported by ICON via NASA's Explorers Program through contracts NNG12FA45C and NNG12FA42I.

References

Achatz, U. (2007). Gravity-wave breaking: Linear and primary nonlinear dynamics. *Advances in Space Research*, *40*(6), 719–733. https://doi.org/10.1016/j.asr.2007.03.078

Amores, A., Monserrat, S., Marcos, M., Argüeso, D., Villalonga, J., Jordà, G., & Gomis, D. (2022). Numerical simulation of atmospheric Lamb waves generated by the 2022 Hunga-Tonga volcanic eruption. *Geophysical Research Letters*, *49*(6), e2022GL098240. https://doi.org/10.1029/2022GL098240

Astafyeva, E., Maletckii, B., Mikesell, T. D., Munaibari, E., Ravanelli, M., Coisson, P., et al. (2022). The 15 January 2022 Hunga Tonga eruption history as inferred from ionospheric observations. *Geophysical Research Letters*, *49*(10), e2022GL098827. https://doi.org/10.1029/2022GL098827

Becker, E., Goncharenko, L., Harvey, V. L., & Vadas, S. L. (2022). Multi-step vertical coupling during the January 2017 sudden stratospheric warming. *Journal of Geophysical Research: Space Physics*, *127*(12), e2022JA030866. https://doi.org/10.1029/2022JA030866

Becker, E., & Vadas, S. L. (2020). Explicit global simulation of gravity waves in the thermosphere. *Journal of Geophysical Research: Space Physics*, *125*(10). https://doi.org/10.1029/2020JA028034

Becker, E., Vadas, S. L., Bossert, K., Harvey, V. L., Zülicke, C., & Hoffmann, L. (2022). A high-resolution whole-atmosphere model with resolved gravity waves and specified large-scale dynamics in the troposphere and stratosphere. *Journal of Geophysical Research: Space Physics*, *127*(2), e2021JD035018. https://doi.org/10.1029/2021JD035018

Carr, J. L., Horváth, Á., Wu, D. L., & Friberg, M. D. (2022). Stereo plume height and motion retrievals for the record-setting Hunga Tonga-Hunga Ha'apai eruption of 15 January 2022. *Geophysical Research Letters*, *49*, e2022GL098131. https://doi.org/10.1029/2022GL098131

Englert, C., Harlander, J., Brown, C., Marr, K. D., Miller, I. J., Stump, J. E., et al. (2017). Michelson Interferometer for Global High-Resolution Thermospheric Imaging (MIGHTI): Instrument design and calibration. *Space Science Reviews*, *212*(1–2), 553–584. https://doi.org/10.1007/s11214-017-0358-4

Forbes, J. M., Bruinsma, S. L., Miyoshi, Y., & Fujiwara, H. (2008). A solar terminator wave in thermosphere neutral densities measured by the CHAMP satellite. *Geophysical Research Letters*, *35*(14), L14802. https://doi.org/10.1029/2008GL034075

Gasque, L. C., Wu, Y.-J., Harding, B. J., Immel, T. J., & Triplett, C. C. (2022). Rapid volcanic modification of the E-region dynamo: ICON's first glimpse of the Tonga eruption. *Geophysical Research Letters*, *49*(18), e2022GL100825. https://doi.org/10.1029/2022GL100825

Gossard, E. E., & Hooke, W. H. (1975). *Waves in the atmosphere* (p. 456). Elsevier Scientific Publishing Co.

Harding, B. J., Chau, J. L., He, M., Englert, C. R., Harlander, J. M., Marr, K. D., et al. (2021). Validation of ICON-MIGHTI thermospheric wind observations: 2. Green-line comparisons to specular meteor radars. *Journal of Geophysical Research: Space Physics*, *126*(3), e2020JA028947. https://doi.org/10.1029/2020JA028947

Harding, B. J., Wu, Y.-J. J., Alken, P., Yamazaki, Y., Triplett, C. C., Immel, T. J., et al. (2022). Impacts of the January 2022 Tonga volcanic eruption on the ionospheric dynamo: ICON-MIGHTI and Swarm observations of extreme neutral winds and currents. *Geophysical Research Letters*, *49*(9), e2022GL098577. https://doi.org/10.1029/2022GL098577

Harding, B. J., Makela, J. J., Englert, C., Marr, K., Harlander, J., England, S., & Immel, T. (2017). The MIGHTI wind retrieval algorithm: Description and verification. *Space Science Reviews*, *212*(1–2), 585–600. https://doi.org/10.1007/s11214-017-0359-3

Huba, J. D., Becker, E., & Vadas, S. L. (2023). Simulation study of the 15 January 2022 Tonga event: Development of super equatorial plasma bubbles. *Geophysical Research Letters*, *50*(1), e2022GL101185. https://doi.org/10.1029/2022GL101185

Lin, J.-T., Rajesh, P. K., Lin, C. C. H., Chou, M.-Y., Liu, J.-Y., Yue, J., et al. (2022). Rapid conjugate appearance of the giant ionospheric Lamb wave signatures in the Northern Hemisphere after Hunga-Tonga volcano eruptions. *Geophysical Research Letters*, *49*(8), e2022GL098222. https://doi.org/10.1029/2022GL098222

Makela, J. J., Baughman, M., Navarro, L. A., Harding, B. J., Englert, C. R., Harlander, J. M., et al. (2021). Validation of ICON-MIGHTI thermospheric wind observations: 1. Nighttime red-line ground-based Fabry-Perot interferometers. *Journal of Geophysical Research: Space Physics*, *126*(2), e2020JA028726. https://doi.org/10.1029/2020JA028726

Miyoshi, Y., Fujiwara, H., Forbes, J. M., & Bruinsma, S. L. (2009). Solar terminator wave and its relation to the atmospheric tide. *Journal of Geophysical Research*, *114*(A7), A07303. https://doi.org/10.1029/2009JA014110

Nishida, K., Kobayashi, N., & Fukao, Y. (2014). Background Lamb waves in the Earth's atmosphere. *Geophysical Journal International*, *196*(1), 312–316. https://doi.org/10.1093/gji/ggt413

Themens, D. R., Watson, C., Žagar, N., Vasylkevych, S., Elvidge, S., McCaffrey, A., et al. (2022). Global propagation of ionospheric disturbances associated with the 2022 Tonga volcanic eruption. *Geophysical Research Letters*, *49*(7), e2022GL098158. https://doi.org/10.1029/2022GL098158

Vadas, S. L. (2013). Compressible *f*-plane solutions to body forces, heatings, and coolings, and application to the primary and secondary gravity waves generated by a deep convective plume. *Journal of Geophysical Research: Space Physics*, *118*(5), 2377–2397. https://doi.org/10.1002/jgra.50163

Vadas, S. L., & Azeem, I. (2021). Concentric secondary gravity waves in the thermosphere and ionosphere over the continental United States on 25–26 March 2015 from deep convection. *Journal of Geophysical Research: Space Physics*, *126*(2), e2020JA028275. https://doi.org/10.1029/2020JA028275

Vadas, S. L., & Fritts, D. C. (2005). Thermospheric responses to gravity waves: Influences of increasing viscosity and thermal diffusivity. *Journal of Geophysical Research*, *110*(D15), D15103. https://doi.org/10.1029/2004JD005574

Vadas, S. L., & Fritts, D. C. (2009). Reconstruction of the gravity wave field from convective plumes via ray tracing. *Annales geophysicae*, *27*, 147–177.

Vadas, S. L., Fritts, D. C., & Alexander, M. J. (2003). Mechanism for the generation of secondary waves in wave breaking regions. *Journal of the Atmospheric Sciences*, *60*(1), 194–214. https://doi.org/10.1029/2004JD005574

Vadas, S. L., & Liu, H.-L. (2009). Generation of large-scale gravity waves and neutral winds in the thermosphere from the dissipation of convectively generated gravity waves. *Journal of Geophysical Research*, *114*(A10), A10310. https://doi.org/10.1029/2009JA014108

Vadas, S. L., Xu, S., Yue, J., Bossert, K., Becker, E., & Baumgarten, G. (2019). Characteristics of the quiet-time hotspot gravity waves observed by GOCE over the Southern Andes on 5 July 2010. *Journal of Geophysical Research: Space Physics*, *124*(8), 7034–7061. https://doi.org/10.1029/2019JA026693

Vadas, S. L., Yue, J., & Nakamura, T. (2012). Mesospheric concentric gravity waves generated by multiple convection storms over the North America Great Plain. *Journal of Geophysical Research*, *117*(D7). https://doi.org/10.1029/2011JD017025

Vadas, S. L., Yue, J., She, C.-Y., Stamus, P., & Liu, A. (2009). A model study of the effects of winds on concentric rings of gravity waves from a convective plume near Fort Collins on 11 May 2004. *Journal of Geophysical Research*, *114*(D6), D06103. https://doi.org/10.1029/2008JD010753

Vadas, S. L., Zhao, J., Chu, X., & Becker, E. (2018). The excitation of secondary gravity waves from local body forces: Theory and observation. *Journal of Geophysical Research: Atmospheres*, *123*(17), 9296–9325. https://doi.org/10.1029/2017JD027970

Wright, C., Hindley, N., Alexander, M. J., Barlow, M., Hoffmann, L., Mitchell, C., et al. (2022). Surface-to-space atmospheric waves from Hunga Tonga-Hunga Ha'apai eruption. *Nature*, *609*, 741–758. https://doi.org/10.1038/s41586-022-05012-5

Zhang, S.-R., Vierinen, J., Aa, E., Goncharenko, L., Erickson, P., Rideout, W., et al. (2022). Tonga volcanic eruption induced global propagation of ionospheric disturbances via Lamb waves. *Frontiers in Astronomy and Space Sciences*, *9*. https://doi.org/10.3389/fspas.2022.871275